An Unconstrained Convex Formulation of Compliant Contact

Alejandro Castro, Frank Permenter, Xuchen Han

***Abstract*—We present a convex formulation of compliant frictional contact and a robust, performant method to solve it in practice. By analytically eliminating contact constraints, we obtain an unconstrained convex problem. Our solver has proven global convergence and warm-starts effectively, enabling simulation at interactive rates. We develop compact analytical expressions of contact forces allowing us to describe our model in clear physical terms and to rigorously characterize our approximations. Moreover, this enables us not only to model point contact, but also to incorporate sophisticated models of compliant contact patches. Our time stepping scheme includes the midpoint rule, which we demonstrate achieves second order accuracy even with frictional contact. We introduce a number of accuracy metrics and show our method outperforms existing commercial and open source alternatives without sacrificing accuracy. Finally, we demonstrate robust simulation of robotic manipulation tasks at interactive rates, with accurately resolved stiction and contact transitions, as required for meaningful sim-to-real transfer. Our method is implemented in the open source robotics toolkit Drake.**

***Index Terms*—Contact Modeling, Simulation and Animation, Dexterous Manipulation, Dynamics.**

I. Introduction

SIMULATION of multibody systems with frictional contact has proven indispensable in robotics, aiding at multiple stages during the mechanical and control design, testing, and training of robotic systems. Robotic applications often require robust simulation tools that can perform at interactive rates without sacrificing accuracy, a critical prerequisite for meaningful sim-to-real transfer. However, reliable modeling and simulation for contact-rich robotic applications remains somewhat elusive.

Rigid body dynamics with frictional contact is complicated by the non-smooth nature of the solutions. It is well known [1] that rigid contact when combined with the Coulomb model of friction can lead to paradoxical configurations for which solutions in terms of accelerations and forces do not exist. These phenomena are known as Painlevé paradoxes [2]. Theory resolves these paradoxes by allowing discrete velocity jumps and impulsive forces, formally casting the problem as a differential variational inequality [3]. In practice, event based approaches can resolve impulsive transitions [4], though it is not clear how to reliably detect these events even for simple one degree of freedom systems [2].

Nevertheless, the problem can be solved in a weaker formulation at the velocity level using a time-stepping scheme where the next step velocities and impulses are the unknowns at each time step [5], [6]. These formulations lead in general to a non-linear complementarity problem (NCP) or to a linear complementarity problem (LCP) when a polyhedral approximations of the friction cone is used. Even though LCP formulations guarantee solution existence [6], [7], solving them accurately and efficiently has remained difficult in practice. This has been explained partly due to the fact that these formulations are equivalent to nonconvex problems in global optimization, which are generally NP-hard [8]. Indeed, popular direct methods based on Lemke's pivoting algorithm to solve LCPs may exhibit exponential worst-case complexity [9]. Similarly, popular iterative methods based on projected Gauss-Seidel (PGS) [10], [11] have also shown exponentially slow convergence [12]. These observations are not just of theoretical value—in practice, these methods are numerically brittle and lack robustness when tasked with computing contact forces. Software typically attempts to compensate for this

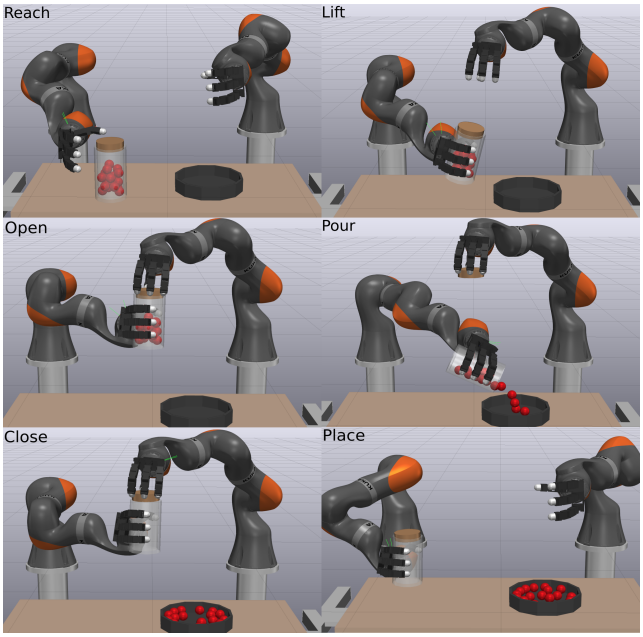

Fig. 1: Keyframes of a dual arm manipulation task in simulation (see supplemental video). The robot is commanded to pick up a jar full of marbles, open it, pour its contents into a bowl, close the lid and place the empty jar back in place. This is a computationally intensive simulation with 160 degrees of freedom and hundreds of contact constraints per time step (see Fig. 18). Our SAP solver is robust and warm-starts effectively, enabling this simulation to run at interactive rates.

All the authors are with Toyota Research Institute, Cambridge, MA, USA, firstname.lastname@tri.global.

inherent lack of stability and robustness through non-physical constraint relaxation and stabilization, requiring a significant amount of application-specific parameter tuning.

To improve computational tractability, Anitescu introduced a *convex relaxation* of the contact problem [13]. This relaxation is a convex approximation with proven convergence to the solution of a measure differential inclusion as the time step goes to zero. For sliding contacts, the convex approximation introduces a *gliding* artifact at a distance ϕ proportional to the time step size δt and to the sliding velocity $\|\boldsymbol{v}_t\|$ [14], i.e. $\phi \sim \delta t\|\boldsymbol{v}_t\|$. The approximation is exact for sticking contacts (dominant in robotic manipulation), and it can be adequate for applications for which the product $\delta t\|\boldsymbol{v}_t\|$ is usually sufficiently small. For trajectory optimization, Todorov [15] introduces regularization into Anitescu's formulation in order to write a strictly convex formulation with a unique, smooth and invertible solution. For simulation, Todorov [16] uses regularization to introduce *numerical compliance* that provides Baumgarte-like stabilization to avoid constraint drift. As a side effect, the regularized formulation can lead to a noticeable non-zero slip velocity even during stiction [17].

Even though these formulations introduce a tractable approximation of frictional contact, they have not been widely adopted in practice. We believe this is because of the lack of robust solution methods with a computational cost suitable for interactive simulation. Software such as ODE [18], Dart [19] and Vortex [20] use a polyhedral approximation of the friction cone leading to an LCP formulation. Algoryx [21] uses a *split solver*, reminiscent of one iteration in the staggered projections method [8]. Drake [22] solves compliant contact with regularized friction with its transition aware solver TAMSI [23].

To our knowledge, Chrono [24] and Mujoco [25] are the only packages that implement the convex approximation of contact. The multi-physics simulation package Chrono implements a variant of the PGS method for solving Anitescu's convex formulation [26]. This method is specially targeted to the simulation of very large scale systems such as those encountered in granular flow. Even though some convergence guarantees are provided in [27], the solver exhibits low convergence rates. This is expected for such a first order method. Mujoco is targeted to robotics and implements both a PGS solver variant [16] and a second order Newton solver. However, the underlying technology is proprietary and implementation details are opaque.

Summarizing, fifteen years after the introduction of these convex approximations, robust and performant algorithms for their solution in practice are lacking. It is not yet clear if these formulations present a real advantage when compared to more traditional approaches and whether the artifacts introduced by the approximation are acceptable in robotics applications. In this work, we aim to provide answers to these questions.

We make a number of novel contributions. To address accuracy and model validity, Section VII provides compact expressions for the impulses that correspond to the optimal velocities of the convex approximation. This provides intuition for the approximation, even to those without optimization expertise. Moreover, the artifacts introduced by the approximation become apparent and can be characterized precisely. In particular, regularization introduced by Todorov [16] is given a clear physical interpretation. Such interpretability allows us to incorporate not only compliant point contact, but also complex models of compliant surface patches [28], as we demonstrate in Section X-D. We introduce in Section IV a time stepping approach based on the θ-method. This includes the popular symplectic Euler method and the implicit midpoint rule. In Section X-B we demonstrate that the midpoint rule can achieve second order accuracy even in problems with frictional contact. Unlike previous work [27], [16] that formulates the problem in its dual form (impulses), we write a primal formulation of compliant contact in velocities (Section V). We then analytically eliminate constraints from this formulation to obtain an unconstrained convex problem (Section VI).

To solve this formulation, we develop SAP—the Semi-Analytic Primal solver—in Section VIII and study its theoretical and practical convergence. Crucially, we show that SAP globally converges from all initial conditions (Appendix F) and warm-starts effectively using the previous time-step velocities, enabling simulation at interactive rates. We provide full details needed for implementation, including formulae for selecting a search direction, a line search procedure, and sparsity analysis. Section IX presents regularization procedures that improve numerical conditioning without sacrificing the accuracy needed for simulation of stiction and simulation of *near-rigid* objects. This is critical for the simulation of demanding robotics tasks such as manipulation. We evaluate the accuracy, robustness and performance of SAP against available commercial and open-source optimization solvers. In Section X, we demonstrate the effectiveness of our approach in a number of simulation cases, including the simulation of the challenging dual arm manipulation task shown in Fig. 1. We discuss extensions and variations in Section XI and conclude with final remarks in Section XII.

II. Multibody Dynamics with Contact

We use generalized coordinates to describe our multibody system. Therefore, the state is fully described by the generalized positions $\mathbf{q} \in \mathbb{R}^{n_q}$ and the generalized velocities $\mathbf{v} \in \mathbb{R}^{n_v}$, where n_q and n_v denote the number of generalized positions and velocities, respectively.

Time derivatives of the generalized positions are described by the kinematic map

$$\dot{\mathbf{q}} = \mathbf{N}(\mathbf{q})\mathbf{v}, \tag{1}$$

where $\mathbf{N}(\mathbf{q}) \in \mathbb{R}^{n_q \times n_v}$ is a block diagonal matrix. For robotic systems comprised of revolute and prismatic joints, the blocks of $\mathbf{N}(\mathbf{q})$ correspond to identity maps. The same is true for deformable body models where the configuration is described by the position of each vertex in a deformable mesh. For systems containing ball joints, free floating bodies, or mobile bases, where either quaternions or Euler angles are used, $\mathbf{N}(\mathbf{q})$ will contain non-identity blocks that are in general functions of the configuration $\mathbf{q}$.

Given a configuration $\mathbf{q}$ of the system, our geometry engine reports a discrete set of n_c contacts between a pair of bodies. The i-th *contact pair* is described by the location $\boldsymbol{p}_i$ of the

contact point, a normal direction $\hat{\boldsymbol{n}}_i$ and the *signed distance* or *gap function* $\phi_i(\mathbf{q}) \in \mathbb{R}$. The kinematics of each contact is further completed with the relative velocity $\boldsymbol{v}_{c,i} \in \mathbb{R}^3$ between these two bodies at point $\boldsymbol{p}_i$, expressed in a contact frame C_i for which we arbitrarily choose the z-axis to coincide with the contact normal $\hat{\boldsymbol{n}}_i$.

We form the vector $\mathbf{v}_c \in \mathbb{R}^{3n_c}$ of contact velocities by stacking velocities $\boldsymbol{v}_{c,i}$ of all contact pairs together. Similarly, we denote by $\boldsymbol{\gamma}_i \in \mathbb{R}^3$ the contact impulse in the contact frame C_i at a specific contact point and with $\boldsymbol{\gamma} \in \mathbb{R}^{3n_c}$ the stacked vector of all contact impulses. In general, unless otherwise specified, we use bold italics for vectors in $\mathbb{R}^3$ and non-italics bold for their stacked counterpart. The generalized velocities $\mathbf{v}$ and contact velocities $\mathbf{v}_c$ satisfy the equation $\mathbf{v}_c = \mathbf{J}\,\mathbf{v}$, where $\mathbf{J}(\mathbf{q}) \in \mathbb{R}^{3n_c \times n_v}$ denotes the contact Jacobian.

To arrive at a discrete time system of equations, we can integrate the momentum balance at intervals of size δt from time step t^n to the next time step $t^{n+1} = t^n + \delta t$. We write this as

$$\mathbf{M}(\mathbf{v}^{n+1} - \mathbf{v}^n) = \delta t\,\bar{\boldsymbol{\tau}} + \mathbf{J}^T\boldsymbol{\gamma}, \tag{2}$$

where $\mathbf{M}(\mathbf{q}) \in \mathbb{R}^{n_v \times n_v}$ is the mass matrix and $\bar{\boldsymbol{\tau}} \in \mathbb{R}^{n_v}$ models external forces such as gravity and gyroscopic terms arising in multibody dynamics. We present a comprehensive discussion of our discrete time-stepping scheme in Section IV.

Denoting with $\gamma_{n,i} \in \mathbb{R}$ and with $\boldsymbol{\gamma}_{t,i} \in \mathbb{R}^2$ the normal and tangential components of the impulse $\boldsymbol{\gamma}_i = [\boldsymbol{\gamma}_{t,i}\,\gamma_{n,i}]$ in frame C_i, the formulation is most often completed with the following set of standard constraints to be satisfied at each contact

1) non-penetration constraint $0 \le \phi_i \perp \gamma_{n,i} \ge 0$,
2) friction cone constraint $\|\boldsymbol{\gamma}_{t,i}\| \le \mu_i\gamma_{n,i}$, where $\mu_i \in \mathbb{R}$ is the coefficient of friction for the i-th contact, and
3) the *maximum dissipation principle*, which states that the friction impulses maximize the rate of energy dissipation. In other words, friction impulses oppose the sliding velocity direction.

Condition 2 states that contact impulses $\boldsymbol{\gamma}_i$ at point i are constrained to belong to the friction cone $\mathcal{F}_i = \{[\boldsymbol{x}_t, x_n] \in \mathbb{R}^3 \,|\, \|\boldsymbol{x}_t\| \le \mu_i x_n\}$.

While these constraints describe the widely used Colulomb friction model, the resulting formulation leads to a very difficult to solve, non-convex, NCP.

III. Convex Approximation of Contact Dynamics

To improve computational tractability and ensure existence of a solution, Anitescu introduces a *convex approximation* of the contact problem [13]. In this approximation, the contact impulses are solutions to the following convex optimization problem

$$\min_{\gamma\in\mathcal{F}} \ell(\boldsymbol{\gamma}) = \frac{1}{2}\boldsymbol{\gamma}^T\mathbf{W}\boldsymbol{\gamma} + \boldsymbol{r}^T\boldsymbol{\gamma}, \tag{3}$$

where $\mathbf{W} = \mathbf{J}\mathbf{M}^{-1}\mathbf{J}^T \in \mathbb{R}^{3n_c\times 3n_c}$ is the *Delassus operator*, $\mathcal{F} := \mathcal{F}_1 \times F_2 \times \cdots \times \mathcal{F}_{n_c}$ is a Cartesian product of friction cones, and $\boldsymbol{r}$ defines a linear cost that encodes external force contributions and stabilization terms used to impose non-penetration at the position level.

Further, [13] uses a polyhedral approximation to linearize the friction cone constraint $\boldsymbol{\gamma}_i \in \mathcal{F}_i$. In this work, we do not linearize the cone constraints, but work directly with the second order cone constraints. This approach is preferred given that the polyhedral approximation is known to introduce non-physical anisotropy [29]. In addition, the linearization of the friction cone results in a far larger problem due to the additional constraints needed to represent the polyhedral cone.

Anitescu shows in [13] that the optimality conditions for the problem in Eq. (3) imply the conservation of momentum in Eq. (2), the maximum dissipation principle, and the modified non-penetration condition

$$0 \le \phi_i - \delta t\|\boldsymbol{v}_{t,i}\| \perp \gamma_{n,i} \ge 0, \tag{4}$$

where $\boldsymbol{v}_{t,i}$ is the tangential component of the contact velocity $\boldsymbol{v}_{c,i} = [\boldsymbol{v}_{t,i}\,v_{n,i}]$. Notice that the modified non-penetration condition in Eq. (4) introduces coupling with the sliding velocity, an artifact of the convex approximation. We provide a detailed discussion on the physical validity of this approximation in Section VII, along with guidelines for determining its applicability to robotic simulation.

In [15], [16] Todorov introduces regularization to the formulation in Eq. (3). Though not strictly applicable to contact problems, the *Gauss's principle of least constraint* is used to obtain the following regularized form of Anitescu's formulation

$$\min_{\gamma\in\mathcal{F}} \ell(\boldsymbol{\gamma}) = \frac{1}{2}\boldsymbol{\gamma}^T(\mathbf{W}+\mathbf{R})\boldsymbol{\gamma} + \boldsymbol{r}^T\boldsymbol{\gamma}, \tag{5}$$

where $\mathbf{R}$ is a diagonal positive matrix introduced to make $\mathbf{W} + \mathbf{R} \succ 0$ since in general we only have $\mathbf{W} \succeq 0$. This makes the problem strictly convex and thus a unique solution exists. Regularization is used as a means to add constraint stabilization with a set of global parameters that control the amount of numerical compliance introduced by the formulation. This is different from our approach described in Section VII, where we show how to use regularization to model physical compliance, with well defined physical parameters.

IV. Discrete Time Formulation

Our discrete-time model is based on the θ-method [30, §II.7]. In particular, it incorporates the symplectic midpoint rule that attains second order accuracy and energy conservation. While most of the work in the literature uses first order time-stepping schemes, the extension to the second-order midpoint rule is analyzed in [31]. In contrast to [31] which uses a polyhedral approximation of the friction cone, our approach does not approximate the friction cone but introduces the convex approximation of contact from [13]. We remark that combining the θ-method with the convex approximation of contact is novel to our work.

We discretize time into intervals of fixed size δt and seek to advance the state of the system from time t^n to the next step at $t^{n+1} = t^n + \delta t$. In the θ-method, variables are evaluated at intermediate time steps $t^\theta = \theta t^{n+1} + (1-\theta)t^n$, with $\theta \in [0, 1]$. We define *mid-step quantities* $\mathbf{q}^{\theta_q}$, $\mathbf{v}^{\theta_v}$, and $\mathbf{v}^{\theta_{vq}}$ in accordance

with the standard θ-method using scalar parameters θ_q, θ_v, and θ_{vq}

$$\begin{aligned}\mathbf{q}^{\theta_q} &= \theta_q\mathbf{q} + (1-\theta_q)\mathbf{q}_0,\\ \mathbf{v}^{\theta_v} &= \theta_v\mathbf{v} + (1-\theta_v)\mathbf{v}_0,\\ \mathbf{v}^{\theta_{vq}} &= \theta_{vq}\mathbf{v} + (1-\theta_{vq})\mathbf{v}_0,\end{aligned} \tag{6}$$

where, to simplify notation, we use $(\mathbf{q}_0, \mathbf{v}_0)$ to denote the state at t^n and $(\mathbf{q}, \mathbf{v})$ to denote the state at t^{n+1}.

Using these mid-step quantities, we write an approximation for the mean generalized forces $\bar{\boldsymbol{\tau}}$ in Eq. (2) as

$$\bar{\boldsymbol{\tau}} = \mathbf{F}_1(\mathbf{q}^{\theta_q}(\mathbf{v}), \mathbf{v}^{\theta_v}(\mathbf{v})) + \mathbf{F}_2(\mathbf{q}^{\theta_q}(\mathbf{v}), \mathbf{v}^{\theta_v}(\mathbf{v})),$$

where we split the forces into two contributions $\mathbf{F}_1$ and $\mathbf{F}_2$ so that the Jacobians $\partial\mathbf{F}_1/\partial\mathbf{q}$ and $\partial\mathbf{F}_1/\partial\mathbf{v}$ are negative definite matrices while the same is generally not true for the Jacobians of $\mathbf{F}_2$. The term $\mathbf{F}_1(\mathbf{q}, \mathbf{v})$ can include forces from modeling elements such as spring and dampers and even internal forces for the modeling of soft-body deformation. The term $\mathbf{F}_2(\mathbf{q}, \mathbf{v})$ includes all other contributions that cannot guarantee negative definiteness of their Jacobians, such as Coriolis and gyroscopic forces arising in multibody dynamics with generalized coordinates.

Using the above definitions, we write our discrete update in the following form

$$\mathbf{m}(\mathbf{v}) = \mathbf{J}(\mathbf{q}^{\theta_q})^T\boldsymbol{\gamma}, \tag{7}$$

$$\mathbf{q} = \mathbf{q}_0 + \delta t\dot{\mathbf{q}}^{\theta_{vq}} = \mathbf{q}_0 + \delta t\mathbf{N}(\mathbf{q}^{\theta_q})\mathbf{v}^{\theta_{vq}}, \tag{8}$$

with the discrete momentum residual $\mathbf{m}(\mathbf{v})$ defined as

$$\mathbf{m}(\mathbf{v}) = \mathbf{M}(\mathbf{q}^{\theta_q}(\mathbf{v}))(\mathbf{v}-\mathbf{v}_0) - \delta t\,\bar{\boldsymbol{\tau}}(\mathbf{q}^{\theta_q}(\mathbf{v}), \mathbf{v}^{\theta_v}(\mathbf{v})), \tag{9}$$

and the kinematic map $\mathbf{N}(\mathbf{q})$ as defined by Eq. (1). Notice that in the update for $\mathbf{q}$ we evaluate $\mathbf{N}$ at t^{θ_q} and velocities at $t^{\theta_{vq}}$. This enables our framework to generalize to some of the most popular schemes for forward dynamics:

- Explicit Euler with $\theta_q = \theta_v = \theta_{vq} = 0$,
- Symplectic Euler with $\theta_q = \theta_v = 0$ and $\theta_{vq} = 1$,
- Implicit Euler with $\theta_q = \theta_v = \theta_{vq} = 1$, and
- Symplectic midpoint rule, which is second order, with $\theta_q = \theta_v = \theta_{vq} = 1/2$,

Similar to the work in [32] for the simulation of deformable objects and to projection methods used in fluid mechanics [33], we solve Eqs. (7) and (8) in two stages. We first solve for the *free motion velocities* the system would have in the absence of contact constraints. We then update the velocities so that they satisfy conservation of momentum along with the contact constraints in the second stage. This two-stage approach is advantageous in that it allows us to choose the most appropriate strategy at each stage. For the update of free motion velocities, we use the θ-method to attain the desired order of accuracy and energy conservation properties, while for the second stage we use our primal formulation of compliant contact presented in Section V to calculate the contact impulses.

In the first stage, we solve for the free motion velocities $\mathbf{v}^*$ in the absence of constraint impulses, i.e.,

$$\mathbf{m}(\mathbf{v}^*) = \mathbf{0}. \tag{10}$$

For integration schemes that are implicit in $\mathbf{v}^*$ (e.g. the implicit Euler scheme and the midpoint rule), we solve Eq. (10) with Newton's method. For schemes explicit in $\mathbf{v}^*$, only the mass matrix $\mathbf{M}$ needs to be inverted, which can be accomplished efficiently using the $\mathcal{O}(n)$ *Articulated Body Algorithm* [34].

In the second stage, we approximately solve Eq. (7) by linearizing $\mathbf{m}(\mathbf{v})$ around $\mathbf{v}^*$. Our linearization uses a symmetric positive definite (SPD) approximation $\mathbf{A}$ of the Jacobian of $\mathbf{m}(\mathbf{v})$ with

$$\mathbf{A} = \mathbf{M} + \delta t^2\,\theta_q\theta_{qv}\mathbf{K} + \delta t\,\theta_v\mathbf{D}, \tag{11}$$

$$\mathbf{K}(\mathbf{q}, \mathbf{v}) = -\frac{\partial\mathbf{F}_1(\mathbf{q}, \mathbf{v})}{\partial\mathbf{q}}\frac{\partial\dot{\mathbf{q}}^{\theta_{vq}}}{\partial\mathbf{v}}, \tag{12}$$

$$\mathbf{D}(\mathbf{q}, \mathbf{v}) = -\frac{\partial\mathbf{F}_1(\mathbf{q}, \mathbf{v})}{\partial\mathbf{v}}, \tag{13}$$

where $\mathbf{K} \succ 0$ and $\mathbf{D} \succ 0$ are the stiffness and damping matrices of the system, respectively. As an example, for joint level spring-dampers models, $\mathbf{K}$ and $\mathbf{D}$ are constant, diagonal, and positive definite matrices. A more complex example arises in the Finite Element Model (FEM) of soft body deformations. In this case, $\mathbf{K}$ and $\mathbf{D}$ are sparse positive definite matrices.

As we will see in Section V, this SPD approximation allows us to write a convex formulation of contact satisfying an approximation of the original momentum balance in Eq. (7),

$$\mathbf{A}(\mathbf{v} - \mathbf{v}^*) = \mathbf{J}^T\boldsymbol{\gamma}. \tag{14}$$

Furthermore, the approximation in Eq. (14) and the original discrete momentum update in Eq. (7) agree to second order as shown by the following result, proved in Appendix A.

Proposition 1. *Matrix* $\mathbf{A}$ *is a first order approximation to the Jacobian of* $\mathbf{m}$*, i.e.,*

$$\left.\frac{\partial\mathbf{m}}{\partial\mathbf{v}}\right|_{\mathbf{v}=\mathbf{v}^*} = \mathbf{A} + \mathcal{O}(\delta t).$$

Therefore, Eq. (14) is a second order approximation of the discrete balance of momentum in Eq. (7). Moreover, $\mathbf{A} \succ 0$.

We summarize our discrete time stepping strategy as follows

1) Solve for the free motion velocities $\mathbf{v}^*$ in Eq. (10).
2) Compute the symmetric positive definite matrix $\mathbf{A}$ in Eq. (11).
3) Solve for constraint impulses $\boldsymbol{\gamma}$ that satisfy the linearized momentum Eq. (14) and the contact constraints.
4) Update the positions according to Eq. (8).

The constraint impulses in step 3 are the solution to our convex approximation of compliant contact described in the next section.

Notice that, in the absence of constraint impulses, the velocities at the next time step are equal to the free motion velocities, i.e., $\mathbf{v} = \mathbf{v}^*$, and they are computed with the order of accuracy of the θ-method. Furthermore, we also expect to recover the properties of the θ-method when contact constraints are not active. As an example, for bodies in contact that are under rolling friction, the contact constraints behave

as bi-lateral constraints that impose zero slip velocity. In this case, our two stage method using the midpoint rule to compute $\mathbf{v}^*$ exhibits considerably less numerical dissipation than other methods. We demonstrate this in Section X-B with an example of a mechanical system with rolling friction.

V. A Primal Formulation of Compliant Contact

In this section we give a convex program that augments the balance of momentum stated in Eq. (14) so that contact impulses model Coulomb friction and satisfy the principle of maximum dissipation. We call this convex program our *primal formulation*, since as stated in Theorem 1, its dual is precisely the formulation stated in Eq. (5). We will see in Section VI that with this primal formulation, we can eliminate the constraints analytically to write an unconstrained convex formulation of the same problem.

We introduce a new decision variable $\boldsymbol{\sigma} \in \mathbb{R}^{3n_c}$ and set up our primal formulation of compliant contact as the following convex optimization problem

$$\begin{aligned} \min_{\mathbf{v},\boldsymbol{\sigma}} \quad & \ell_p(\mathbf{v},\boldsymbol{\sigma}) = \frac{1}{2}\|\mathbf{v}-\mathbf{v}^*\|_A^2 + \frac{1}{2}\|\boldsymbol{\sigma}\|_R^2 \\ \text{s.t.} \quad & \mathbf{g} = (\mathbf{J}\mathbf{v} - \hat{\mathbf{v}}_c + \mathbf{R}\boldsymbol{\sigma}) \in \mathcal{F}^*, \end{aligned} \tag{15}$$

where $\|\mathbf{z}\|_X^2 = \mathbf{z}^T\mathbf{X}\mathbf{z}$ with $\mathbf{X} \succ 0$ and $\mathcal{F}^* = \mathcal{F}_1^* \times \mathcal{F}_2^* \times \cdots \times \mathcal{F}_{n_c}^*$ is the *dual cone* of the friction cone $\mathcal{F}$. The positive diagonal matrix $\mathbf{R} \in \mathbb{R}^{3n_c\times 3n_c}$ and the vector of stabilization velocities $\hat{\mathbf{v}}_c$ encode the problem data needed to model compliant contact. We will establish a very clear physical meaning for these terms when we provide analytical expressions for the impulses in Section VII. In the limit of rigid contact when the regularization $\mathbf{R}$ is zero, our primal formulation reduces to that presented in [14].

We conclude this section with the following theorem, proved in Appendix B.

Theorem 1. *The dual of* (15) *is given by* (5)*. Moreover, when* $\{\mathbf{v},\boldsymbol{\sigma}\}$ *is primal optimal and* $\boldsymbol{\gamma}$ *is dual optimal,* $\boldsymbol{\sigma} = \boldsymbol{\gamma}$*.*

An important outcome from the proof of Theorem 1 is that the optimality condition for the primal formulation (15) corresponds to the balance of momentum, Eq. (14). That is, the convex program (15) encodes both balance of momentum and contact constraints.

VI. An Unconstrained Convex Formulation

Remarkably, the dual optimal impulses of (5) can be constructed from the primal optimal velocities of (15) using a simple projection operation. Following [16], we call this construction *inverse dynamics*. Moreover, this projection decomposes into a set of individual projections for each contact impulse $\boldsymbol{\gamma}_i$ given the separable structure of the constraints. Letting $\boldsymbol{y}_i(\boldsymbol{v}_{c,i}) = -\boldsymbol{R}_i^{-1}(\boldsymbol{v}_{c,i} - \hat{\boldsymbol{v}}_{c,i})$, these projections take the form

$$\begin{aligned} \boldsymbol{\gamma}_i(\boldsymbol{v}_{c,i}) &= P_{\mathcal{F}_i}(\boldsymbol{y}_i(\boldsymbol{v}_{c,i})) \\ &= \arg\min_{\boldsymbol{\gamma}\in\mathcal{F}_i} \quad \frac{1}{2}(\boldsymbol{\gamma}-\boldsymbol{y}_i)^T\boldsymbol{R}_i(\boldsymbol{\gamma}-\boldsymbol{y}_i), \end{aligned} \tag{16}$$

where $\boldsymbol{R}_i \in \mathbb{R}^{3\times 3}$ is the i-th diagonal block of the regularization matrix $\mathbf{R}$. That is, $\boldsymbol{\gamma}_i$ is the projection $P_{\mathcal{F}_i}$ of $\boldsymbol{y}_i(\boldsymbol{v}_{c,i})$ onto the friction cone $\mathcal{F}_i$ using the norm defined by $\boldsymbol{R}_i$. The projection $P_{\mathcal{F}}(\mathbf{y})$ onto the full cone $\mathcal{F} := \mathcal{F}_1 \times F_2 \times \cdots \times \mathcal{F}_{n_c}$ is obtained by simply stacking together the individual projections $P_{\mathcal{F}_i}(\boldsymbol{y}_i)$ from Eq. (16), where we form $\mathbf{y}$ by stacking together each $\boldsymbol{y}_i$ from all contact pairs. In this notation, the optimal impulse $\boldsymbol{\gamma}$ of (5) and the optimal velocities $\mathbf{v}$ of (15) satisfy $\boldsymbol{\gamma} = P_{\mathcal{F}}(\mathbf{y}(\mathbf{v}))$.

We use $\boldsymbol{\gamma} = P_{\mathcal{F}}(y(\mathbf{v}))$ and the optimality condition $\sigma = \boldsymbol{\gamma}$ from Theorem 1 to eliminate both σ and the constraints from the primal formulation. In total, we obtain the following unconstrained problem in velocities only

$$\min_{\mathbf{v}} \ell_p(\mathbf{v}) = \frac{1}{2}\|\mathbf{v}-\mathbf{v}^*\|_A^2 + \frac{1}{2}\|P_{\mathcal{F}}(\mathbf{y}(\mathbf{v}))\|_R^2. \tag{17}$$

Correctness of this reformulation is asserted by the following theorem, which we prove in Appendix C.

Theorem 2. *If* $\mathbf{v}$ *solves the unconstrained formulation (17), then* $(\mathbf{v},\boldsymbol{\sigma})$*, with* $\boldsymbol{\sigma} = P_{\mathcal{F}}(\mathbf{y}(\mathbf{v}))$*, solves the primal formulation (15).*

Lemma 2 in Appendix F shows that the unconstrained cost $\ell_p(\mathbf{v})$ is strongly convex and differentiable with Lipschitz continuous gradients. Therefore, the unconstrained formulation (17) has a unique solution, and can be efficiently solved. Section VIII presents our novel SAP solver specifically designed for its solution.

VII. Compliant Contact, Principle of Maximum Dissipation and Artifacts

Thus far, $\boldsymbol{R}_i$ and $\hat{\boldsymbol{v}}_{c,i}$ have been treated as known problem data. This section makes an explicit connection of these quantities with physical parameters to model compliant contact with regularized friction. Notice this approach is different from the one in [16], where regularization is not used to model physical compliance but rather to introduce a user tunable Baumgarte-style stabilization to avoid constraint drift. We want to model compliant contact with stiffness k (in N/m) and linear dissipation $c = \tau_d k$ where τ_d (in seconds) is the *dissipation time scale*.

Dropping subscript i for simplicity, we solve the projection problem in Eq. (16) analytically in Appendix D for a regularization matrix of the form $\boldsymbol{R} = \text{diag}([R_t, R_t, R_n])$

$$\begin{aligned} \boldsymbol{\gamma} &= P_{\mathcal{F}}(\boldsymbol{y}) \\ &= \begin{cases} \boldsymbol{y} & \text{stiction, } y_r \le \mu y_n \\ \begin{bmatrix} \mu\gamma_n\hat{\boldsymbol{t}} \\ \frac{1}{1+\hat{\mu}^2}(y_n + \hat{\mu}y_r) \end{bmatrix} & \text{sliding, } -\hat{\mu}y_r < y_n \le \dfrac{y_r}{\mu} \\ \mathbf{0} & \text{no contact, } y_n < -\hat{\mu}y_r \end{cases} \end{aligned} \tag{18}$$

where $\boldsymbol{y}_t$ and y_n are the tangential and normal components of $\boldsymbol{y}$, $y_r = \|\boldsymbol{y}_t\|$ is the radial component, and $\hat{\boldsymbol{t}} = \boldsymbol{y}_t/y_r$ is the unit tangent vector. We also define the coefficients $\tilde{\mu} = \mu\,(R_t/R_n)^{1/2}$ and $\hat{\mu} = \mu\,R_t/R_n$ that result from the *warping* introduced by the metric $\boldsymbol{R}$.

Our compliant model of contact is defined by

$$\begin{aligned}\hat{\boldsymbol{v}}_c &= \begin{bmatrix}0\\0\\\hat{v}_n\end{bmatrix},\\ \hat{v}_n &= -\frac{\phi_0}{\delta t+\tau_d},\end{aligned}$$

where ϕ_0 is the previous step signed distance. The normal direction regularization parameters is taken as $R_n^{-1}=\delta t k(\delta t+\tau_d)$. To gain physical insight into our model, we substitute $\boldsymbol{y}=-\boldsymbol{R}^{-1}(\boldsymbol{v}_c-\hat{\boldsymbol{v}}_c)$ into Eq. (18) to obtain

$$\boldsymbol{\gamma}(\boldsymbol{v}_c)=P_{\mathcal{F}}(\boldsymbol{y}(\boldsymbol{v}_c))$$
$$=\begin{cases}\begin{bmatrix}-\boldsymbol{v}_t/R_t\\-\delta t(k\phi+cv_n)\end{bmatrix} & \text{stiction},\\ \begin{bmatrix}\mu\gamma_n\hat{\boldsymbol{t}}\\-\frac{\delta t}{1+\tilde{\mu}^2}\left(k(\phi-(\delta t+\tau_d)\mu\|\boldsymbol{v}_t\|)+cv_n\right)\end{bmatrix} & \text{sliding},\\ \mathbf{0} & \text{no contact},\end{cases}$$

where $\phi=\phi_0+\delta t\, v_n$. Let us now analyze the resulting forces from this model.

A. Friction Forces

We see that friction forces behave exactly as a model of regularized friction

$$\boldsymbol{\gamma}_t=\min\left(\frac{\|\boldsymbol{v}_t\|}{R_t},\mu\gamma_n\right)\hat{\boldsymbol{t}},$$

with $\boldsymbol{\gamma}_t$ linear to the (very small) slip velocity during stiction and with a maximum value given by $\mu\gamma_n$, effectively modeling Coulomb friction. Notice that to better model stiction, we are interested in small values of R_t. We discuss our parameterization of R_t in Section IX. Moreover, since $\hat{\boldsymbol{t}}=\boldsymbol{y}_t/\|\boldsymbol{y}_t\|=-\boldsymbol{v}_t/\|\boldsymbol{v}_t\|$, friction forces oppose sliding and therefore satisfy the principle of maximum dissipation.

B. Normal Forces

We observe that in stiction, normal forces model compliance with linear stiffness k and linear dissipation $c=\tau_d k$. That is

$$\gamma_n/\delta t=-k\phi-cv_n.$$

In the sliding region, however, we see that the convex approximation introduces unphysical artifacts.

Firstly, the factor $1+\tilde{\mu}^2$ models an effective stiffness $k_{\text{eff}}=k/(1+\tilde{\mu}^2)$ and dissipation $c_{\text{eff}}=c/(1+\tilde{\mu}^2)$, different from the physical values. This tell us that in order to accurately model compliance during sliding we must satisfy the condition $\tilde{\mu}=\mu\,(R_t/R_n)^{1/2}\approx 0$ or, equivalently, $R_t\ll R_n$. Section IX introduces a parameterization of R_t that satisfies this condition.

Secondly, while we'd like to recover $\gamma_n=-\delta t(k\phi+cv_n)$ as in stiction, we instead see that the slip velocity $\boldsymbol{v}_t$ unphysically couples into the normal forces as $\gamma_n=-\delta t(k(\phi-(\delta t+\tau_d)\mu\|\boldsymbol{v}_t\|)+cv_n)$. We can write this as

$$\gamma_n/\delta t=-(k\phi_{\text{eff}}+cv_n),$$

with an *effective* signed distance $\phi_{\text{eff}}=\phi-(\delta t+\tau_d)\mu\|\boldsymbol{v}_t\|$. That is, we recover the dynamics of compliant contact but with a spurious drift of magnitude $(\delta t+\tau_d)\mu\|\boldsymbol{v}_t\|$.

This is consistent with the formulation in [27] for rigid contact when $k\to\infty$ and $\tau_d=0$, leading to an unphysical *gliding effect* at a positive distance $\phi=\delta t\mu\|\boldsymbol{v}_t\|$. Notice that the *gliding* goes away as $\delta t\to 0$ since the formulation converges to the original contact problem [13]. The effect of compliance is to *soften* this gliding effect.

With finite compliance, the normal force when sliding goes to $-k(\phi-\tau_d\mu\|\boldsymbol{v}_t\|)$ in the limit to $\delta t\to 0$. This tells us that, unlike the rigid case, the *gliding* effect unfortunately does not go away as $\delta t\to 0$. It persists with a finite value that now depends on the dissipation rate, $\phi\approx\tau_d\mu\|\boldsymbol{v}_t\|$.

We close this discussion by making the following remarks relevant to robotics applications:

1) We are mostly interested in the stiction regime, typically for grasping, locomotion, or rolling contact for mobile bases with wheels. This regime is precisely where the convex approximation does not introduce artifacts.
2) Sliding usually happens with low velocities and therefore the term $\delta t\mu\|\boldsymbol{v}_t\|$ is negligible.
3) For robotics applications, we are mostly interested in inelastic contact. We will see that this can be effectively modeled with $\tau_d\approx\delta t$ in Section IX. Therefore, in this regime, the term $\tau_d\mu\|\boldsymbol{v}_t\|$ also goes to zero as $\delta t\to 0$.
4) We are definitely interested in the onset of sliding. This is captured by the approximation which properly models the Colulomb friction law.

VIII. Semi-Analytic Primal Solver

Inspired by Newton's method, our Semi-Analytic Primal Solver (SAP) seeks to monotonically decrease the primal cost $\ell_p(\mathbf{v})$ at each iteration, as outlined in Algorithm 1

Algorithm 1 The Semi-Analytic Primal Solver (SAP)

1: Initialize $\mathbf{v}_m\leftarrow\mathbf{v}_0$
2: **repeat until** $\|\tilde{\nabla}\ell_p\|<\varepsilon_a+\varepsilon_r\max(\|\tilde{\mathbf{p}}\|,\|\tilde{\mathbf{j}}_c\|)$, Eq. (20)
3: $\quad\Delta\mathbf{v}_m=-\mathbf{H}^{-1}(\mathbf{v}_m)\nabla_{\mathbf{v}}\ell_p(\mathbf{v}_m)$
4: $\quad\alpha_m=\arg\min_{t\in\mathbb{R}^{++}}\ell_p(\mathbf{v}_m+t\Delta\mathbf{v}_m)$
5: $\quad\mathbf{v}_{m+1}=\boldsymbol{v}_m+\alpha_m\Delta\mathbf{v}_m$
6: **return** $\{\mathbf{v},\boldsymbol{\gamma}=P_{\mathcal{F}}(\boldsymbol{y}(\mathbf{v}))\}$

The SAP iterations require $\mathbf{H}(\mathbf{v})\succ 0$ at all iterations. At points where $\nabla_{\mathbf{v}}\ell_p(\mathbf{v})$ is differentiable, $\mathbf{H}(\mathbf{v})$ is simply set equal to the Hessian of the cost function. In general, $\mathbf{H}(\mathbf{v})$ is evaluated using a partition of its domain. For each set in the partition, $\nabla_{\mathbf{v}}\ell_p(\mathbf{v})$ is differentiable on the interior, and the Hessian admits a simple formula. Outside the interior, we evaluate $\mathbf{H}(\mathbf{v})$ by using the Hessian formula derived for the interior. This procedure provides a globally valid definition for $\mathbf{H}(\mathbf{v})$. The partition is described in Appendix D. The Hessian formula are given in Appendix E. Our convergence analysis in Appendix F also accounts for this definition.

As shown in Appendix F, SAP globally convergences at least at a linear-rate. Further, SAP exhibits quadratic convergence when $\nabla^2\ell_p$ exists in a neighborhood of the optimal $\mathbf{v}$. In

practice, we initialize SAP with the previous time-step velocity $\mathbf{v}_0$. The stopping criteria is discussed below in Section VIII-E.

A. Gradients

We provide a detailed derivation of the gradients in Appendix E. Here we summarize the main results required for implementation. The gradient of the primal cost ℓ_p reduces to the balance of momentum

$$\nabla_{\mathbf{v}}\ell_p(\mathbf{v}) = \mathbf{A}(\mathbf{v}-\mathbf{v}^*) - \mathbf{J}^T\boldsymbol{\gamma}(\mathbf{v}),$$

where $\boldsymbol{\gamma}(\mathbf{v}) = P_{\mathcal{F}}(\boldsymbol{y}(\mathbf{v}))$ is given by the analytical inverse dynamics (18). We define matrix $\mathbf{G} \succeq 0$ that evaluates to $-\nabla_{\mathbf{v}_c}\boldsymbol{\gamma}$ where $P_{\mathcal{F}}(\mathbf{y}(\mathbf{v}))$ is differentiable. Otherwise $\mathbf{G}$ extends our analytical expressions as outlined in Appendix E. Matrix $\mathbf{G}$ is a block diagonal matrix where each diagonal block for the i-th contact is a 3×3 matrix.

In total, we evaluate $\mathbf{H}$ via

$$\mathbf{H} = \mathbf{A} + \mathbf{J}^T\mathbf{G}\,\mathbf{J},$$

which is strictly positive definite since $\mathbf{A} \succ 0$.

B. Line Search

The line search algorithm is critical to the success of SAP given that $\nabla\ell_p(\mathbf{v})$ can rapidly change during contact-mode transitions. We explore two line search algorithms: an approximate backtracking line search with Armijo's stopping criteria and an exact (to machine epsilon) line search.

At the m-th Newton iteration, backtracking line search starts with a maximum step length of α_{Max} and progressively decreases it by a factor $\rho \in (0,1)$ as $\alpha \leftarrow \rho\alpha$ until Armijo's criteria [35, §3.1] is satisfied. We write Armijo's criteria as $\ell_p(\mathbf{v}^m + \alpha\Delta\mathbf{v}^m) < \ell_p(\mathbf{v}^m) + c\,\alpha\, d\ell_p/d\alpha(\mathbf{v}^m)$. Typical parameters we use are $\rho = 0.8$, $c = 10^{-4}$ and $\alpha_{\text{Max}} = 1.5$.

For the exact line search we use the method `rtsafe` [36, §9.4] to find the unique root of $d\ell/d\alpha$. This is a one-dimensional root finder that uses the Newton-Raphson method and switches to bisection when an iterate falls outside a search bracket or when convergence is slow. The fast computation of derivatives we show next allows us to iterate α to machine precision at a negligible impact on the computational cost. In practice, this is our preferred algorithm since it allows us to use very low regularization parameters without having to tune tolerances in the line search. Moreover, we observe 15%-35% performance improvement when compared to the backtracking line search.

C. Efficient Analytical Derivatives For Line Search

The algorithm `rtsafe` requires the first and second directional derivatives of ℓ_p, while the backtracking method only requires the first derivative to verify Armijo's stopping criteria. We show how to compute these derivatives efficiently in $\mathcal{O}(n)$ operations. Defining $\ell(\alpha) = \ell_p(\mathbf{v}+\alpha\Delta\mathbf{v})$, we compute first and second derivatives as

$$\frac{d\ell}{d\alpha} = \Delta\mathbf{v}^T\nabla_{\mathbf{v}}\ell(\alpha),$$
$$\frac{d^2\ell}{d\alpha^2} = \Delta\mathbf{v}^T\mathbf{H}(\alpha)\Delta\mathbf{v}.$$

Using the gradients from Section VIII-A, we can write

$$\frac{d\ell}{d\alpha}(\alpha) = \Delta\mathbf{v}^T\mathbf{A}(\mathbf{v}(\alpha)-\mathbf{v}^*) - \Delta\mathbf{v}^T\mathbf{J}^T\boldsymbol{\gamma}.$$

These are computed efficiently by first calculating the change in velocity $\Delta\mathbf{v}_c := \mathbf{J}\Delta\mathbf{v}$ and change of momentum $\Delta\mathbf{p} := \mathbf{A}\Delta\mathbf{v}$. The calculation is then completed via

$$\frac{d\ell}{d\alpha}(\alpha) = \Delta\mathbf{p}^T(\mathbf{v}(\alpha)-\mathbf{v}^*) - \Delta\mathbf{v}_c^T\boldsymbol{\gamma}(\alpha),$$

which only requires dot products that can be computed in $\mathcal{O}(n_v)$ and $\mathcal{O}(n_c)$ respectively. Similarly for the second derivatives

$$\frac{d^2\ell}{d\alpha^2}(\alpha) = \Delta\mathbf{v}^T\Delta\mathbf{p} + \Delta\mathbf{v}_c^T\mathbf{G}\Delta\mathbf{v}_c.$$

Notice the first term on the right can be precomputed before the line search starts, while the second term only involves $\mathcal{O}(n_c)$ operations given the block diagonal structure of $\mathbf{G}$.

D. Problem Sparsity

The matrix $\mathbf{H}$ inherits a block sparse structure from the specific contact configuration of the problem. We exploit this structure using a supernodal Cholesky factorization [37, §9]. Implementing this factorization requires construction of a *junction tree*. For this we apply the algorithm in [38], using cliques of $\mathbf{H}$ as input. We use the implementation from the Conex solver [39].

The block sparsity of $\mathbf{H}$ is best described with an example. We organize our multibody systems as a collection of articulated *tree structures*, or a *forest*. Consider the system in Fig. 2. In this example, a robot arm mounted on a mobile

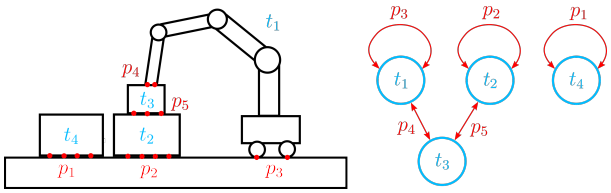

Fig. 2: An example of a sparsity pattern commonly encountered in the simulation of robotic mechanical systems. The graph on the right puts *trees* as nodes and contact *patches* as edges.

base constitutes its own tree, here labeled t_1. The number of degrees of freedom of the t-th tree will be denoted with n_t. A free body is the common case of a tree with $n_t = 6$. In general, matrix $\mathbf{A}$ has a block diagonal structure where each diagonal block corresponds to a tree.

We define as *patches* a collection of contact pairs between two trees. Each contact pair corresponds to a single cone constraint in our formulation. The set of constraint indexes that belong to patch p is denoted with $\mathcal{I}_p$ of size (cardinality) $|\mathcal{I}_p| = r_p$. Figure 2 shows the corresponding graph where nodes correspond to trees and edges correspond to patches.

Generally, the Jacobian is sparse since the relative contact velocity only involves velocities of two trees in contact. When rows are condensed by patches and columns by trees, the

Jacobian exhibits a sparse block structure. Figure 3 illustrates the Jacobian sparsity for the example in Fig. 2, where each non-zero block is the Jacobian $\mathbf{J}_{pt}$ of size $3r_p \times n_t$.

Finally, since $\mathbf{A}$ is block diagonal, $\mathbf{H}$ inherits the sparsity structure of $\mathbf{J}^T\mathbf{G}\mathbf{J}$. For our example, this is sketched in 3. Notice how the sparsity pattern of $\mathbf{J}^T\mathbf{G}\mathbf{J}$ exactly matches the graph from Fig. 2. Using this block structure, our supernodal Cholesky factorization can take full advantage of specific optimizations for dense algebra.

E. Stopping Criteria

To assess convergence, we monitor the norm of optimality condition for the unconstrained problem (17)

$$\nabla \ell_p(\mathbf{v}) = \mathbf{A}(\mathbf{v} - \mathbf{v}^*) - \mathbf{J}^T\boldsymbol{\gamma}.$$

Notice that the components of $\nabla\ell_p$ have units of generalized momentum $\mathbf{p} = \mathbf{M}\mathbf{v}$. Depending on the choice of generalized coordinates, the generalized momentum components may have different units. In order to weigh all components equally, we define the diagonal matrix $\mathbf{D} = \text{diag}(\mathbf{M})^{-1/2}$ and perform the following change of variables

$$\begin{aligned}\tilde{\nabla}\ell_p &= \mathbf{D}\nabla\ell_p,\\ \tilde{\mathbf{p}} &= \mathbf{D}\mathbf{p},\\ \tilde{\mathbf{j}}_c &= \mathbf{D}\mathbf{j}_c,\end{aligned} \tag{19}$$

where we defined the generalized contact impulse $\mathbf{j}_c = \mathbf{J}^T\boldsymbol{\gamma}$. With this scaling, all the new *tilde* variables have the same units, square root of Joules. Using these definitions, we write our stopping criteria as

$$\|\tilde{\nabla}\ell_p\| < \varepsilon_a + \varepsilon_r \max(\|\tilde{\mathbf{p}}\|, \|\tilde{\mathbf{j}_c}\|). \tag{20}$$

where ε_r is a dimensionless relative tolerance that we usually set in the range from 10^{-6} to 10^{-1}. The absolute tolerance ε_a is used to detect rare cases where the solution leads to no contact and no motion, typically due to external forces. We always set this tolerance to a small number, $\varepsilon_a = 10^{-16}$.

IX. Understanding Model Parameters

We have provided explicit algebraic expressions for the impulses as a function of contact velocities in Eq. (18) via the inverse dynamics. While these expressions are given in terms of regularization $\mathbf{R}$, Section VII describes in detail the resulting physical model in terms of contact stiffness k, dissipation time constant τ_d and friction coefficient μ. Therefore, users of this model only need to provide these physical parameters and regularization is computed from them.

Regularization parameters not only determine the physical model, but also affect the robustness and performance of the SAP solver. Modeling near-rigid objects and avoiding viscous drift during stiction require very small values of R_t and R_n that can lead to badly ill-conditioned problems. Under these conditions, the Hessian of the system exhibits a large condition number, and round-off errors can render the search direction of Newton iterations useless. We show in this section how a judicious choice of the regularization parameters leads to much better conditioned system of equations, without sacrificing accuracy.

A. Near-Rigid Contact

With the formulation presented in this work, all bodies are modeled as compliant. Therefore, rigid objects must be modeled as *near-rigid* bodies with large stiffness. However, as mentioned above, blindly choosing large values of stiffness can lead to ill-conditioned systems of equations. Here, we propose a principled way to choose the stiffness parameter when modeling near-rigid contact.

Consider the dynamics of a mass particle m laying on the ground, with contact stiffness k and dissipation time scale τ_d. When in contact, the dynamics of this particle is described by the equations of a harmonic oscillator with natural frequency $\omega_n^2 = k/m$, or period $T_n = 2\pi/\omega_n$, and damping ratio $\zeta = \tau_d\omega_n/2$. We say the contact is *near-rigid* when $T_n \lesssim \delta t$ and the time step δt cannot temporally resolve the contact dynamics.

In this *near-rigid* regime, we use compliance as a means to add a Baumgarte-like *stabilization* to avoid constraint drift, as similarly done in [15]. Choosing the time scale of the contact to be $T_n = \beta\delta t$ with $\beta \le 1$, we model inelastic contact with a dissipation that leads to a critically damped oscillator, or $\zeta = 1$. This dissipation is $\tau_d = 2\zeta/\omega_n$, or in terms of the time step,

$$\tau_d = \frac{\beta}{\pi}\delta t.$$

Using the harmonic oscillator equations, we can estimate the value of stiffness from the frequency ω_n as $k = 4\pi^2 m/(\beta^2\delta t^2)$. Since $\tau_d \approx \delta t$, $R_n^{-1} = \delta t k(\delta t + \tau_d) \approx \delta t^2 k$, and we estimate the regularization parameter as

$$R_n = \frac{\beta^2}{4\pi^2}\text{w},$$

where we defined $\text{w} = 1/m$.

It is useful to estimate the amount of penetration for a point mass resting on the ground. In this case we have

$$\begin{aligned}\phi &= \frac{mg}{k},\\ &= \frac{\beta^2}{4\pi^2} m\text{w} g\delta t^2,\\ &= \frac{\beta^2}{4\pi^2} g\delta t^2,\end{aligned}$$

independent of mass. Taking $\beta = 1.0$ and Earth's gravitational constant, a typical simulation time step of $\delta t = 10^{-3}$ s leads to $\phi \approx 2.5 \times 10^{-7}$ m, and a large simulation time step of $\delta t = 10^{-2}$ s leads to $\phi \approx 2.5 \times 10^{-5}$ m, well within acceptable bounds to consider a body rigid for typical robotics applications.

For a general multibody system, we define the per-contact effective mass as $\text{w}_i = \|\mathbf{W}_{ii}\|_{\text{rms}} = \|\mathbf{W}_{ii}\|/3$ where $\mathbf{W}_{ii}$ is the 3×3 diagonal block of the Delassus operator $\mathbf{W} = \mathbf{J}\mathbf{M}^{-1}\mathbf{J}^T$ for the i-th contact. Explicitly forming the Delassus operator is an expensive operation. Instead we use an $\mathcal{O}(n)$ approximation. Given contact i involving trees t_1 and t_2, we form the approximation $\mathbf{W}_{ii} \approx \mathbf{J}_{it_1}\mathbf{M}_{t_1}^{-1}\mathbf{J}_{it_1}^T + \mathbf{J}_{it_2}\mathbf{M}_{t_2}^{-1}\mathbf{J}_{it_2}^T$. Using this approximation, we estimate the frequency of the contact dynamics as $\omega_n = \sqrt{k\text{w}_i}$.

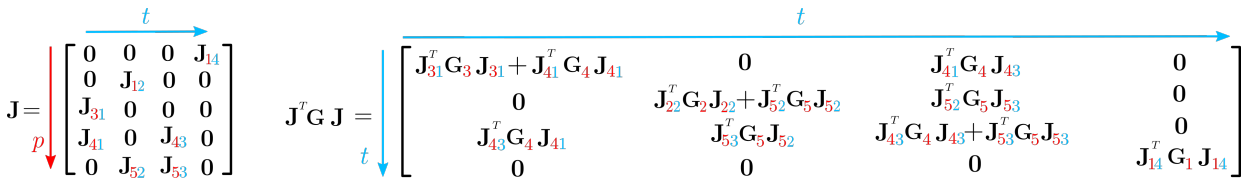

Fig. 3: Block sparsity of the contact Jacobian $\mathbf{J}$ and the Hessian term $\mathbf{J}^T\mathbf{G}\mathbf{J}$, for the example illustrated in Fig. 2.

Finally, we compute the regularization parameter in the normal direction as

$$R_n = \max\left(\frac{\beta^2}{4\pi^2}\|\mathbf{W}_{ii}\|_{\text{rms}}, \frac{1}{\delta t k(\delta t + \tau_d)}\right). \tag{21}$$

With this strategy, our model automatically switches between modeling compliant contact with stiffness k when the time step δt can resolve the temporal dynamics of the contact, and using stabilization to model near-rigid contact with the amount of stabilization controlled by parameter β. In all of our simulations, we use $\beta = 1.0$.

B. Stiction

Given that our model regularizes friction, we are interested in estimating a bound on the slip velocity at stiction. We propose the following regularization for friction

$$R_t = \sigma \mathrm{w}, \tag{22}$$

where σ is a dimensionless parameter.

To understand the effect of σ in the approximation of stiction, we consider once again a point of mass m in contact with the ground under gravity, for which $\mathrm{w} \approx 1/m$. We push the particle with a horizontal force of magnitude $F = \mu\gamma_n$ so that friction is right at the boundary of the friction cone and the slip velocity due to regularization, v_s, is maximized. Then in stiction, we have

$$\|\boldsymbol{\gamma}_t\| = \frac{v_s}{R_t} = \mu m g \delta t.$$

Using our proposed regularization in Eq. (22), we find the maximum slip velocity

$$v_s \approx \mu\sigma g \delta t, \tag{23}$$

independent of the mass and linear with the time step size. Even though the friction coefficient μ can take any non-negative value, most often in practical applications $\mu < 1$. Values in the order of 1 are in fact considered as large friction values. Therefore, for this analysis we consider $\mu \approx 1$. In all of our simulations, we use $\sigma = 10^{-3}$. With Earth's gravitational constant, a typical simulation with time step of $\delta t = 10^{-3}$ s leads to a stiction velocity of $v_s \approx 10^{-5}$m/s, and with a large step of $\delta t = 10^{-2}$ s, $v_s \approx 10^{-4}$ m/s. Smaller friction coefficients lead to even tighter bounds. These values are well within acceptable bounds even for simulation of grasping tasks, which are significantly more demanding than simulation for other robotic applications, see Section X.

C. Sliding Soft Contact

As we discussed in Section VII, we require $R_t/R_n \ll 1$ so that we model compliance accurately during sliding. Now, in the *near-rigid* contact regime, the condition $R_t/R_n \ll 1$ is no longer required since in this regime regularization is only used to apply stabilization and avoid constraint drift. Therefore, we only need to verify this condition in the *soft contact* regime, when time step δt can properly resolve the contact dynamics, i.e. according to our criteria, when $\delta t < T_n$. In this regime, $R_n^{-1} \approx \delta t^2 k$, and using Eq. (22) we have

$$\frac{R_t}{R_n} \approx \sigma \delta t^2 \omega_n^2 = 4\pi^2 \sigma \left(\frac{\delta t}{T_n}\right)^2 \lesssim 4\pi^2\sigma$$

where in the last inequality we used the assumption that we are in the soft regime where $\delta t < T_n$. Since $\sigma \ll 1$ and in particular we use $\sigma = 10^{-3}$ in all of our simulations, we see that $R_t/R_n \ll 1$. Moreover, R_t/R_n goes to zero quadratically with $\delta t/T_n$ as the time step is reduced and the dynamics of the compliance is better resolved in time.

Therefore, we have shown that our choice of regularization parameters enjoys the following properties

1) Users only provide physical parameters; contact stiffness k, dissipation time scale τ_d, and friction coefficient μ. There is no need for users to tweak solver parameters.
2) In the *near-rigid* limit, our regularization in Eq. (21) automatically switches the method to model rigid contact with constraint stabilization to avoid excessively large stiffness parameters and the consequent ill-conditioning of the system.
3) Frictional regularization is parameterized by a single dimensionless parameter σ. We estimate a bound for the slip velocity during stiction to be $v_s \approx \mu\sigma\delta t g$. For $\sigma = 10^{-3}$, the slip during stiction is well within acceptable bounds for robotics applications.
4) We show that $R_t/R_n \ll 1$ when δt can resolve the dynamics of the compliant contact, as required to accurately model compliance during sliding.

In addition, our tests cases in Section X show that this choice of regularization parameters keeps the condition number of the Hessian at each Newton iteration under control.

X. Test Cases

We evaluate the robustness, accuracy, and performance of our method in a number of simulation tests. All simulations are carried out in a system with 24 2.2 GHz Intel Xeon cores (E5-2650 v4) and 128 GB of RAM, running Linux. However, all of our tests are run in a single thread.

For all of our simulations, unless otherwise specified, our model uses $\beta = 1.0$ and $\sigma = 10^{-3}$ for the regularization parameters in Eq. (21) and Eq. (22), respectively.

A. Performance Comparisons Against Other Solvers

We evaluate commercial software Gurobi, considered an industry standard, to solve our primal formulation (15). As an open source option, we evaluate the Geodesic interior-point method (IPM) from [39]. Geodesic IPMs, in contrast with primal-dual IPMs, do not apply Newton's method to the central-path conditions directly. Instead, they use geodesic curves that satisfy the complementarity slackness condition. Since the Geodesic IPM and SAP use the same supernodal linear algebra code described in Section VIII-D, it is natural to compare their performance.

For performance comparisons, we use the steady clock from the STL `std::chrono` library to measure wall-clock time for SAP and Geodesic IPM. For Gurobi we access the `Runtime` property reported by Gurobi. Notice this is somewhat unfair to SAP and Geodesic IPM since Gurobi's reported time does not include the cost of the initial setup.

B. Spring-Cylinder

We model the setup shown in Fig. 4, consisting of a cylinder of radius $R = 0.05$ m and mass $m = 0.5$ kg connected to a wall to its left by a spring of stiffness $k_s = 100$ N/m. While the cylinder is free to rotate and translate in the plane, the ground constrains the cylinder's motion in the vertical direction. The contact stiffness is $k = 10^4$ N/m and the dissipation time scale is $\tau_d = 0.02$ s. The cylinder is initially placed with zero velocity at $x_0 = 0.1$ m to the right of the spring's resting position, and it is then set free.

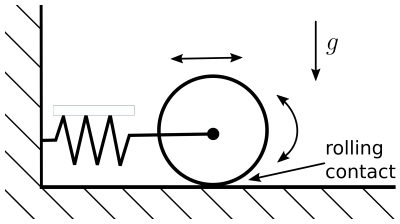

Fig. 4: Spring-Cylinder system. The cylinder can translate horizontally and rotate. Friction with the ground establishes a non-dissipative rolling contact.

For reference, we first simulate this setup with frictionless contact, i.e. $\mu = 0$. Without friction, the cylinder does not rotate and we effectively have a spring-mass system with natural frequency $\omega_n = \sqrt{k_s/m}$. We use a rather coarse time step of $\delta t = 0.02$ s, discretizing each period of oscillation with about 22 steps. Figure 5 shows the total mechanical energy as a function of time computed using three different schemes; symplectic Euler, midpoint rule, and implicit Euler. The amount of numerical dissipation introduced by the implicit Euler scheme dissipates the initial energy in just a few periods of oscillation. For the symplectic Euler scheme, we observe in Fig. 5 that, while the energy is not conserved, it stays bounded, within a band 28% peak-to-peak wide. The figure also confirms that the second order midpoint scheme conserves energy exactly. These are well known theoretical properties of these integration schemes when applied to the spring-mass system.

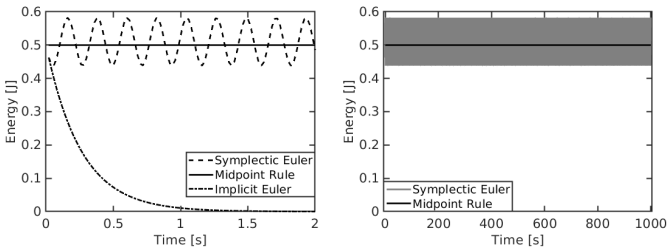

Fig. 5: Total mechanical energy for the frictionless spring-cylinder system in the first few periods of oscillation (left) and long term (right).

We now focus our attention to a case with frictional contact using $\mu = 1$. As we release the cylinder from its initial position at $x_0 = 0.1$ m, friction with the ground establishes a rolling contact, and the system sets into periodic motion. Since now kinetic energy is split into translational and rotational components, the rolling cylinder behaves as a spring-mass system with an effective mass $m_{\text{eff}} = m + I_o/R^2$, with I_o the rotational inertia of the cylinder about its center. Therefore the frequency of oscillation is slower and the same time step, $\delta t = 0.02$ s, now discretizes one period of oscillation with about 27 steps.

Total energy is shown in Fig. 6. Solutions computed with the implicit Euler and the symplectic Euler schemes show similar trends to those in the frictionless case. The midpoint rule does not conserve energy exactly but it does significantly better, with a peak-to-peak variation of only 0.16%. While the ideal rolling contact does not dissipate energy, the regularized model of friction does dissipate energy given the slip velocity is never exactly zero, though small in the order of $\sim \sigma\mu\delta t g$ as shown in Section VII. The symplectic Euler scheme and the midpoint rule take 10 minutes of simulated time and about 1000 oscillations to dissipate 10% of the total energy (Fig. 6, right). This level of numerical dissipation is remarkably low, considering that real mechanical systems often introduce several sources of dissipation.

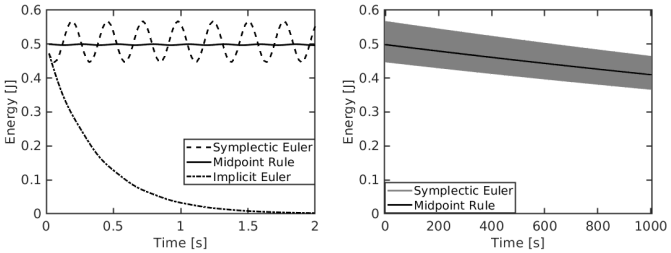

Fig. 6: Total mechanical energy for the spring-cylinder system with friction $\mu = 1$ in the first few periods of oscillation (left) and long term (right).

To study the order of accuracy of our approach, we define the L^2-norm position error as

$$e_q = \left(\frac{1}{T} \int_0^T dt (x(t) - x_e(t))^2 \right)^{1/2}$$

where $x_e(t)$ is the known exact solution. We simulate for $T = 5$s, about 10 periods of oscillation. Figure 7 shows the position error as a function of the time step. We see that even with frictional contact, the two-stage approach with the midpoint rule achieves second order of accuracy. Both the implicit Euler and the symplectic Euler schemes are first order, though the error is significantly smaller when using the symplectic Euler scheme.

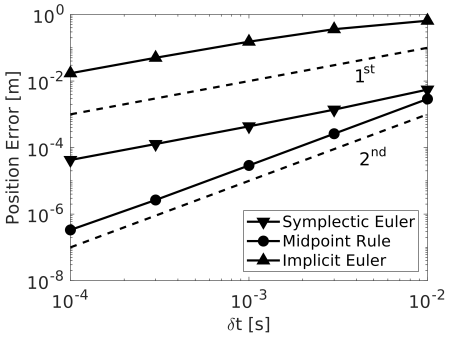

Fig. 7: Position error as a function of time step for the spring-cylinder system with friction. First and second order references are shown with dashed lines.

C. Clutter

Objects are dropped into an 80 cm×80 cm×80 cm container in four different columns with the same number of objects each (see Fig. 8). Each column consists of an arbitrary assortment of spheres of radius 5 cm and boxes with sides of 10 cm in length. With a density of 1000kg/m^3, spheres have a mass of 0.524 kg and boxes have a mass of 1.0 kg. We set a very high contact stiffness of $k = 10^{12}$ N/m so that the model is in the *near-rigid* regime. The dissipation time scale is set to equal the time step and the friction coefficient of all surfaces is $\mu = 1.0$.

We first run our simulations with 10 bodies per column for a total of 40 bodies. We simulate 10 seconds using time steps of size $\delta t = 10$ ms. Number of solver iterations and wall-clock time per time step are reported in Fig. 9. We observe that SAP needs to perform a larger number of iterations during the very energetic initial transient. As the system reaches a steady state, however, SAP warm starts very effectively, performing only about 3 iterations per time step. Even though SAP necessities a larger number of iterations to converge than Geodesic IPM during this initial transient, the wall-clock time per time step is very similar. Unlike SAP and Geodesic IPM that benefit from warm start, we see that Gurobi performs about 9 iterations per time step in both the initial transient and the steady state.

Figure 10 shows two examples of convergence history. We denote with ℓ^0 to the cost evaluated at the initial guess, the previous time step velocity. With ℓ_* we denote the optimal cost, which we approximate with its value from the last iteration. At step 60 during the initial transient for which SAP requires 21 iterations to converge, we observe that the algorithm reaches quadratic convergence after an initial linear convergence transient, matching theoretical predictions

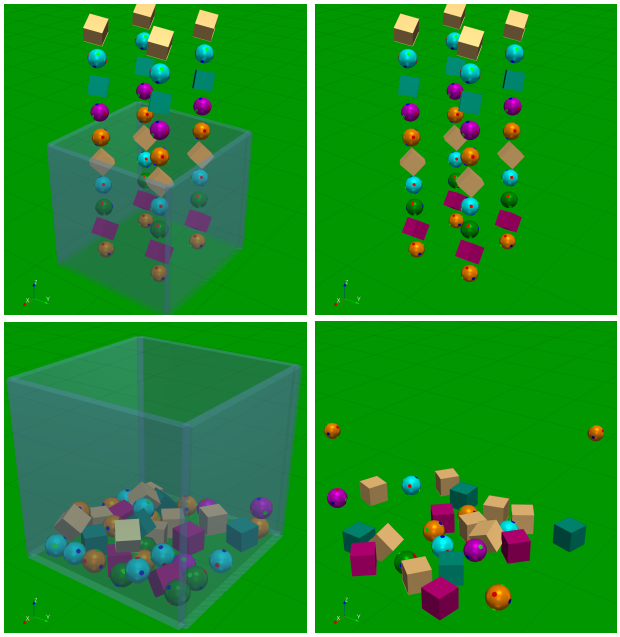

Fig. 8: Initial conditions (top) and an intermediate configuration after 2 seconds of simulated time (bottom) for the clutter setup with (left) and without (right) walls. Many of the spheres in the configuration with no walls roll outside the frame in the intermediate configuration.

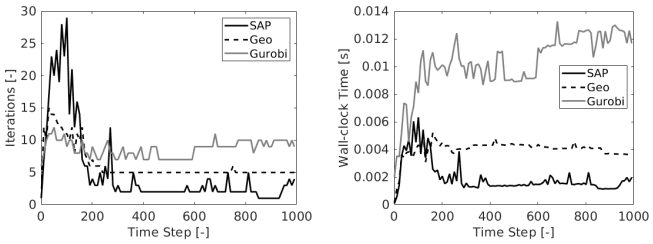

Fig. 9: Iterations and wall-clock time per time step for the clutter case with 40 bodies and with walls.

(Appendix F). At step 520, past the initial energetic transient, SAP exhibits linear convergence and satisfies the convergence criteria within 5 iterations.

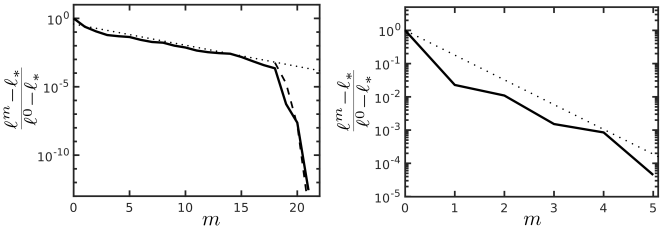

Fig. 10: Cost as a function of Newton iterations for step 60 (left) and for step 520 (right) using SAP. The cost decreases monotonically. Reference lines are shown for linear convergence (dotted) and quadratic convergence (dashed).

1) Scalability: We evaluate the scalability of SAP by varying the number of objects in the clutter. We study the case with and without walls (see Fig. 8) as this variation

leads to very different contact configurations and sparsity patterns. The size of the problems can be appreciated in Fig. 11 showing the number of contact constraints at the end of the simulation when objects are in steady state. We observe a larger number of contacts for the configuration without walls since in this configuration many of the boxes spread over the ground and lay flat on one of their faces, leading to multi-contact configurations (see Fig. 8).

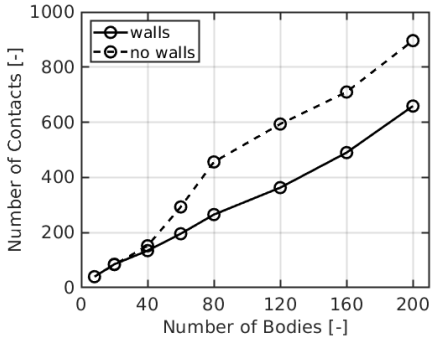

Fig. 11: Total number of contacts with objects in steady state at the end of the simulation for setups with and without walls.

We define the *speedup* against Gurobi as the ratio of the wall-clock time spent by a solver to the wall-clock time reported by Gurobi. Figure 12 shows the speedup for both SAP and Geodesic IPM in the configuration with and without walls. The setup with walls is particularly difficult given that objects are constrained to pile up, leading to a configuration in which almost all objects are coupled with every other object by frictional contact (see Fig. 8). That is, the motion of an object at the bottom of the pile can lead to motion of another object far on top of the pile. In contrast, the simulation with no walls leads to *islands* of objects that do not interact with each other.

In general, we observe two regimes. For problems with less than about 40 bodies, SAP outperforms Gurobi significantly by up to a factor of 25 in the case with walls and up to a factor of 50 with no walls. Beyond 80 bodies, Gurobi outperforms both SAP and Geodesic IPM in the case with walls, but SAP is about 10 times faster for the case with no walls. Though SAP shows to be about twice as fast as Geodesic IPM for most problem sizes, it can be five times faster for small problems with 8 bodies or less.

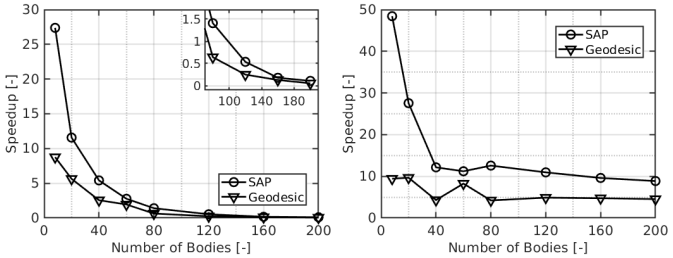

Fig. 12: Speedup against Gurobi for the configuration with walls (left) and without walls (right).

It could be argued that these speedup results depend on the accuracy settings of each solver. For a fair comparison, we define the dimensionless momentum error as

$$e_m = \frac{\|\tilde{\nabla}\ell_p\|}{\max(\|\tilde{\mathbf{p}}\|, \|\tilde{\mathbf{j}_c}\|)}, \tag{24}$$

using the scaled generalized momentum quantities in Eq. (19). We also define the dimensionless complementarity slackness error as

$$e_\mu = \frac{1/n_c \sum_i |\boldsymbol{g}_i \cdot \boldsymbol{\gamma}_i|}{\ell_p}. \tag{25}$$

Figure 13 shows average values of e_m and e_μ over all time steps. Since SAP satisfies the complementarity slackness exactly, e_μ is not shown. We have verified this to be true within machine precision for all simulated cases.

SAP's momentum error is below 10^{-5} as expected since this is the value used for the termination condition. Similarly, the complementarity slackness is below 10^{-5} for Geodesic IPM, since this is the value used for its own termination condition. Gurobi does a good job at satisfying the complementarity slackness. However, it is the solver with the largest error in the momentum equations, even though both SAP and Geodesic IPM outperform Gurobi in most of the test cases. These metrics demonstrate that when SAP and Geodesic IPM outperform Gurobi, it is not at the expense of accuracy.

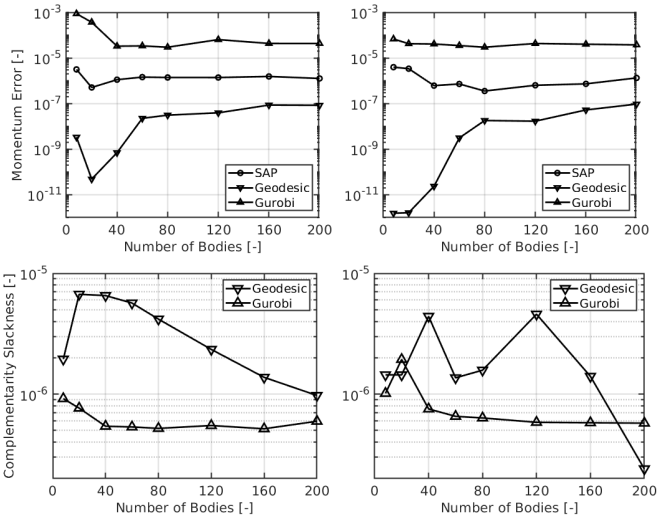

Fig. 13: Momentum balance error e_m (top) and complementarity condition error e_μ (bottom) for the clutter case with walls (left) and without walls (right).

2) Slip Parameter: We study the effect of the slip parameter σ in Eq. (22). We use $\delta t = 10$ ms and simulate with SAP 40 objects for 10 seconds to a steady state configuration. At this steady state, we compute the mean slip velocity among all contacts, shown in Fig. 14 along with the estimated slip in Eq. (23), $v_s \approx \sigma\mu\delta t g$. We see that the mean slip velocity remains below the estimated slip as expected in a static configuration with objects in stiction. In the case with walls where stiction helps to hold the steady state static configuration, we see that the mean slip velocity closely follows the slope of the slip estimate. Without the walls, objects do not pile up in a

complex static structure but simply lie on the ground, and therefore, the resulting slip velocities are significantly smaller. The sudden drop in the slip velocity for $\sigma > 10^{-3}$ is caused by the sensitivity of the final state on the value of σ. As σ increases, so does the slip velocity bound v_s and objects in the configuration without walls can slowly drift into a configuration leading to more contacts. In particular, boxes are more likely to slowly drift until one of their faces lies flat on the ground, a configuration with zero slip once steady state is reached.

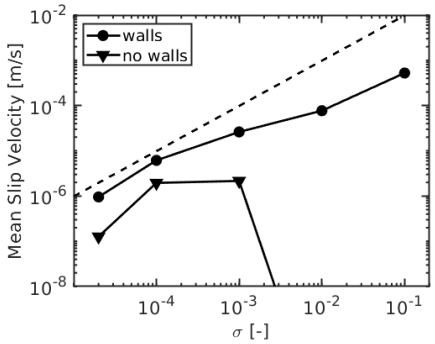

Fig. 14: Mean slip velocity at the end of the simulation with objects at rest as a function of the slip parameter. The estimated bound $v_s = \sigma\mu\delta t g$ is shown in dashed lines.

We conclude by examining the effect of σ on the conditioning of the system. Figure 15 shows the condition number of the Hessian in the final configuration and the mean number of Newton iterations throughout the simulation. We see that the condition number scales as σ^{-1} while the mean number of Newton iterations is roughly proportional to $\ln(\sigma)$. Our default choice $\sigma = 10^{-3}$ is a good compromise between accurate stiction, performance and conditioning.

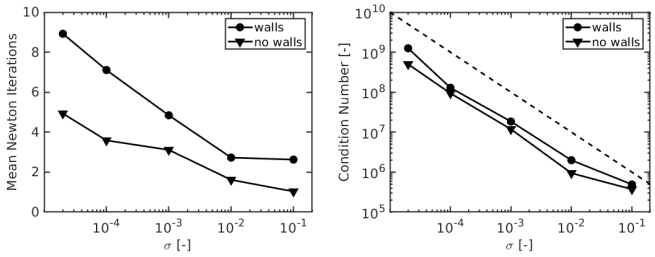

Fig. 15: Effect of the slip parameter on the mean Newton iterations per step (left) and mean condition number (right).

D. Slip Control

While previous work on convex approximations model rigid contact [13], [14] or use regularization as a means of constraint stabilization [16], our work is novel in that we incorporate physical compliance. This allows us not only to model compliant point contact, but also to incorporate sophisticated models of surfaces patches. We incorporate the pressure field model [28] implemented as part of Drake's [22] *hydroelastic contact* model. We use the discrete approximation introduced in [40] to approximate each face of the contact surface as a compliant element at its centroid.

To demonstrate this capability, we reproduce the test in [40] that models a *Soft-bubble* gripper [41]; a parallel jaw WSG 50 Schunk gripper outfitted with air filled compliant surfaces. The aforementioned gripper is simulated anchored to the world holding a spatula by the handle horizontally. We use $\delta t = 5 \times 10^{-3}$ s. The grasp force is commanded to vary between 1 N and 16 N with square wave having a 6 second period and a 75% duty cycle, left on Fig. 17. This results in a periodic transition from a secure grip to a loose grip allowing the spatula to pitch in a controlled manner within grasp, see Fig. 17 and the accompanying video. We observe that stiction during the secure grip is properly resolved with the tight bounds for the slip due to regularization discussed in Section IX-B. While this case only has 8 degrees of freedom, it generates about 60 contact constraints during the slip phase and about 160 contact constraints during the stiction phase.

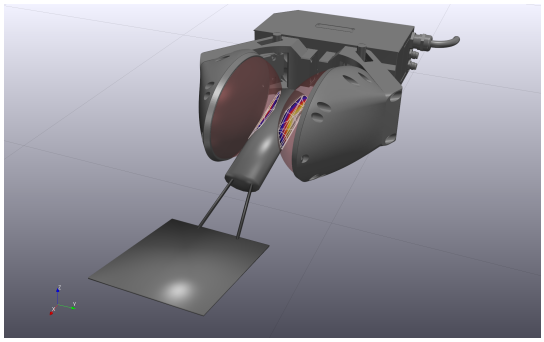

Fig. 16: Highly compliant *Soft-bubble* gripper [41] holding a spatula. Unlike traditional point contact approaches, the hydroelastic contact model provides rich contact information and captures area-dependent phenomena such as the net-torque to hold the spatula. Contact patches are colored by contact pressure.

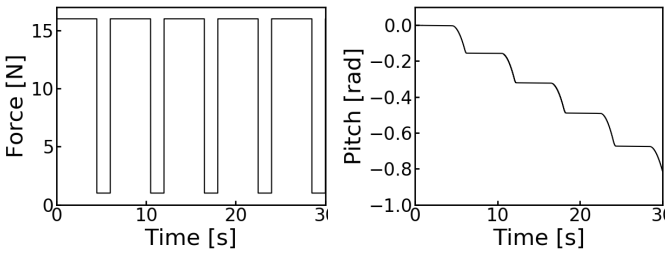

Fig. 17: Grip force command (left) and spatula pitch angle (right) as a function of time.

We compare the performance of SAP against both Gurobi and Geodesic IPM, see Section X-A. For SAP we use a relative tolerance $\varepsilon_r = 10^{-3}$, see Section VIII-E. For Gurobi we set its tolerance parameter `BarQCPConvTol` to 10^{-8}. For Geodesic IPM, we set its complementary slackness tolerance to 10^{-6}; larger values lead to failure for this task. SAP bounds the momentum error, exhibiting a maximum value of of $9.99 \times 10^{-2}\,\%$. Even with such a tight tolerance, Gurobi

exhibits 2.6 % maximum error. Geodesic IPM's errors are significantly smaller, below 2×10^{-4} %. However its robustness is very sensitive to the specified tolerance.

Even though SAP's solutions are significantly more accurate than those from Gurobi, it performs 92 times faster than Gurobi. SAP is 20 times faster than Geodesic IPM and significantly more robust to solver tolerances. In terms of solver iterations, SAP only performs 0.62 iterations on average, showcasing how effectively it warm-starts. Geodesic IPM performs 5.6 iterations per step on average and Gurobi performs 10.1 iterations on average.

E. Dual Arm Manipulation

We demonstrate the effectiveness of our approach with the simulation of a complex manipulation task. In this scenario, two Kuka IIWA arms (7 DOFs each) are outfitted with anthropomorphic Allegro hands (16 DOFs each), see Fig. 1. In front of the robot, a table has a jar (with a lid, 12 DOFs) full of 16 marbles of 50 gr each (96 DOFs) and a bowl (6 DOFs), completing the model with a total of 160 DOFs. Contact between the jar and the lid is modeled using Drake's hydroelastic model [28], [40] (see Section X-D), while point contact is used for all other interactions. The time step is set to $\delta t = 5 \times 10^{-3}$ s.

The arms' controllers track a prescribed sequence of Cartesian end-effector keyframe poses, while the hands' controllers track prescribed *open/close* configurations. We use force feedback to gauge successful grasps and to know when the jar makes contact with the table. The robot is commanded to open the jar, pour its contents into the bowl, close the lid and put the empty jar back in place, see keyframes in Fig. 1 and the accompanying video.

This particular task generates hundreds of contact constraints, as shown in Fig. 18 which also labels important events during the task.

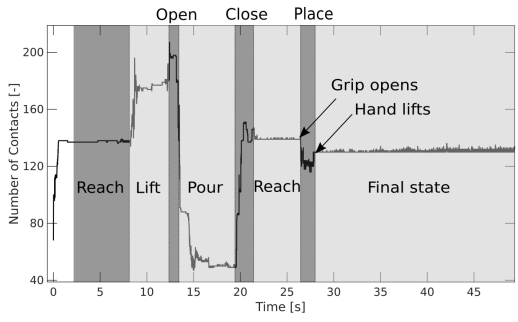

Fig. 18: Number of contact constraints as a function time. Important events during the task are highlighted.

To assess accuracy, we evaluate the dimensionless momentum and complementarity slackness errors defined in Eqs. (24) and (25) respectively. We perform the simulation of the same task several times using different solver tolerances. The results of these runs are shown in Figures 19 and 20. Even though each solver uses a different tolerance parameter, it is still useful to place these tolerances in the same horizontal axis. The maximum tolerance we use for each solver corresponds to the largest value that can be used to complete the task successfully. For Gurobi and Geodesic IPM, smaller values of the tolerance parameter make the simulation impractically slow. SAP on the other hand cannot achieve errors below 10^{-6} for this case due to round-off errors. Figures 19 and 20 show both mean and median of the errors over the entire simulation to show errors do not follow a symmetric distribution. More interesting however are the minimum and maximum errors, shown as shaded areas. SAP guarantees that momentum errors are below the specified tolerance, given this is precisely its stopping criteria in Eq. (20). We see however that it is difficult to correlate the expected error to solver tolerance when using Gurobi or Geodesic IPM. In practice, we consistently observed that the simulation did not complete the task successfully when momentum errors were larger than about 10%, regardless of the solver. Therefore, we found that being able to specify a tolerance for the momentum error directly is immensely useful. Given that SAP satisfies the complementarity slackness condition exactly, complementarity slackness error for SAP is not included in Fig. 20.

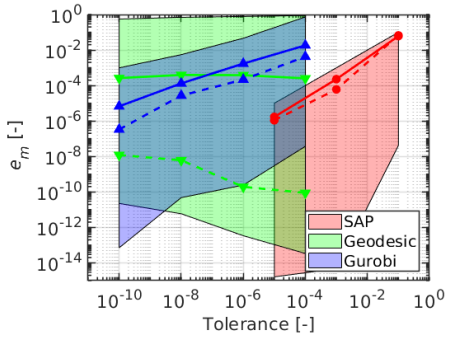

Fig. 19: Dimensionless momentum error, defined in Eq. (24). Mean (solid) and median (dashed) errors along with minimum and maximum errors (shaded areas) over the entire simulation.

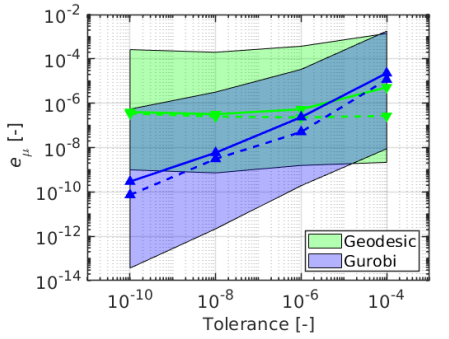

Fig. 20: Dimensionless complementarity slackness error, defined in Eq. (25). Mean (solid) and median (dashed) errors along with minimum and maximum errors (shaded areas) over the entire simulation.

Figure 21 shows the mean number of iterations per time-step for each solver. We see that the number of iterations needed by the SAP solver is consistently below the other two solvers given how effectively SAP warm-starts from the previous time-step solution.

To make a fair comparison among solvers, from Fig. 19 we choose tolerances for each solver that result in similar values of the mean momentum error. For Gurobi we set its tolerance parameter `BarQCPConvTol` to 10^{-8}, for Geodesic IPM, we set its complementary slackness tolerance to 10^{-6} and for SAP its relative tolerance is set to 10^{-3}. Notice this is not entirely fair to SAP, given that SAP does guarantee the maximum momentum error to be below 10^{-3}, while this is not true for the other two solvers. Still, SAP is 7.4 faster than Gurobi and 2.2 faster than Geodesic IPM. In terms of iterations, SAP performs 4 iterations on average while Geodesic IPM performs 8.3 iterations on average. This shows that since both solvers use exactly the same sparse algebra, the performance gains with SAP are entirely due to its ability to warm-start effectively rather than to differences in the implementation. The general purpose solver Gurobi on the other hand performs 10.1 iterations on average.

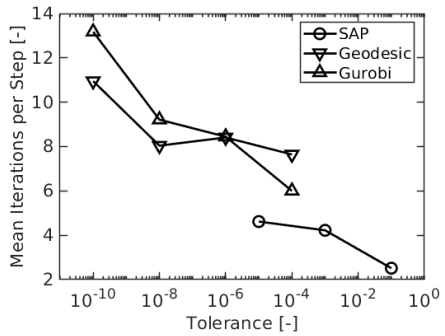

Fig. 21: Mean number of iterations per time-step for the dual arm simulation.

In summary, the simulation of this complex robotic task demonstrates how accuracy translates directly to robustness. We observed how the maximum momentum error defined in Eq. (24) is a good proxy for robustness in simulation; simulations with errors larger than about 10% could not complete the task successfully. In this regard SAP provides a certificate of accuracy that proves useful in practice.

XI. Variations and Extensions

The method presented in this paper can be extended in several ways:

Expand the family of constraints: No doubt contact constraints are the most challenging. However, our method can be extended to include bilateral constraints, PD controllers with force limits and even joint dry friction [16].

Branch induced sparsity: In this work we exploit sparsity only at a tree level. However, branch sparsity can lead to additional performance. Consider for instance a humanoid robot with a floating hip. Since arms and upper torso are not in contact with the ground, they can be eliminated from the computation in terms of degrees of freedom in the legs. Additional performance gains could be attained using specialized algebra for multibody dynamics [42].

Parallelization: This work focuses on the accuracy, robustness, and convergence properties of the algorithm executed in a single thread. The sparse algebra can be parallelized and, in particular, disjoints *islands* of bodies can be solved separately in different threads.

Deformable FEM models: Section IV gives a glimpse into this topic. However, deformable objects introduce a much larger number of unknowns and require specialized handling of sparsity.

Differentiation: Since forces are a continuous function of state, the model is well suited for applications requiring gradients such as trajectory optimization, machine learning, parameter estimation, and control. Factorizations computed during forward dynamics can be reused when computing gradients for a performant implementation.

XII. Conclusion

We presented a formulation of compliant contact with a novel physics-based parameterization. We showed that forces can be succinctly described by analytical expressions with a clear physical intuition. This allowed us to incorporate not only point contact but also more complex models of surface patches. We then showed that when these forces are used in the momentum equations, we obtain the optimality conditions for an unconstrained convex formulation. We made a rigorous presentation of the numerical approximations and a novel characterization of the artifacts introduced by the convex approximation of contact; the approximation is exact for sticking contact and introduces an $\mathcal{O}(\delta t\|\boldsymbol{v}_t\|)$ *gliding* effect for sliding contact.

We developed a two-stage time stepping approach based on the θ-method and we showed that with the midpoint rule it can achieve second order accuracy even in problems with frictional contact. Our formulation does not linearize the friction cone but it works with the second order cone constraints directly.

We presented SAP, a robust and performant open source solver for this formulation that warm-starts very effectively in practice. SAP globally converges at least at a linear-rate and exhibits quadratic convergence when additional smoothness conditions are satisfied. We showed that SAP exhibits these two convergence regimes in simulations of practical relevance. We provided thorough details for implementation, including analytical formulae for gradients and Hessian, sparsity analysis and custom line search.

We compared the performance of SAP against commercial and open source optimization solvers. Using quantitative accuracy metrics we showed that SAP outperforms the alternatives not only without sacrificing accuracy, but even at higher accuracy and added robustness. SAP can be up to 50 times faster than Gurobi in small problems with up to a dozen objects and up to 10 times faster in medium sized problems with about 100 objects. Even though SAP uses the supernodal algebra implemented for Geodesic IPM, it performs at least two times faster due to its effective warm-starts from the previous time-step solution. Moreover, SAP is significantly more robust in practice given that it guarantees a hard bound on the error in momentum, effectively providing a certificate of accuracy.

We have incorporated SAP into the open source robotics toolkit Drake [22], and hope that the simulation and robotics communities can benefit from our contribution.

APPENDIX A
PROOF OF PROPOSITION 1

The Taylor expansion of $\mathbf{m}(\mathbf{v})$ at $\mathbf{v}=\mathbf{v}^*$ reads

$$\begin{aligned}\mathbf{m}(\mathbf{v}) &= \mathbf{m}^* + \frac{\partial \mathbf{m}}{\partial \mathbf{v}}(\mathbf{v}-\mathbf{v}^*) + \mathcal{O}_m(\|\mathbf{v}-\mathbf{v}^*\|^2) \\ &= \frac{\partial \mathbf{m}}{\partial \mathbf{v}}(\mathbf{v}-\mathbf{v}^*) + \mathcal{O}_m(\|\mathbf{v}-\mathbf{v}^*\|^2), \end{aligned} \tag{26}$$

where we use the fact that by definition $\mathbf{m}^* = \mathbf{m}(\mathbf{v}^*) = \mathbf{0}$. All derivatives are evaluated at $\mathbf{v}=\mathbf{v}^*$ unless otherwise noted. We first evaluate the Jacobian of the mass matrix term in Eq. (9)

$$\frac{\partial \left(\mathbf{M}(\mathbf{q}^{\theta_q}(\mathbf{v}))(\mathbf{v}-\mathbf{v}_0)\right)}{\partial \mathbf{v}} = \mathbf{M}(\mathbf{q}^{\theta_q}(\mathbf{v}^*)) + \mathbf{E},$$

where we defined

$$\mathbf{E} = \frac{\partial \mathbf{M}(\mathbf{q}^{\theta_q})}{\partial \mathbf{v}}(\mathbf{v}^*-\mathbf{v}_0).$$

Note that by combining Eqs. (6) and (8), the mid-step configuration $\mathbf{q}^{\theta_q}$ can be written as

$$\begin{aligned}\mathbf{q}^{\theta_q}(\mathbf{v}) &= \mathbf{q}_0 + \delta t \theta_q \dot{\mathbf{q}}^{\theta_{vq}} \\ &= \mathbf{q}_0 + \delta t \theta_q \mathbf{N}(\mathbf{q}^{\theta_q})\mathbf{v}^{\theta_{vq}}(\mathbf{v}).\end{aligned}$$

Hence by the chain rule, $\mathbf{E}$ can be further calculated as

$$\mathbf{E} = \delta t \theta_q \frac{\partial \mathbf{M}(\mathbf{q}^{\theta_q})}{\partial \mathbf{q}} \frac{\partial \dot{\mathbf{q}}^{\theta_{vq}}}{\partial \mathbf{v}}(\mathbf{v}^*-\mathbf{v}_0).$$

Notice that

$$\begin{aligned}\|\mathbf{E}\| &\leq \delta t \theta_q \left\| \frac{\partial \mathbf{M}(\mathbf{q}^{\theta_q})}{\partial \mathbf{q}} \right\| \left\| \frac{\partial \dot{\mathbf{q}}^{\theta_{vq}}}{\partial \mathbf{v}} \right\| \|\mathbf{v}^*-\mathbf{v}_0\| \\ &= \mathcal{O}(\delta t^2),\end{aligned}$$

since $\|\mathbf{v}^*-\mathbf{v}_0\| = \mathcal{O}(\delta t)$.

We proceed similarly to expand the Jacobian of $\mathbf{F}_1(\mathbf{v}) = \mathbf{F}_1(\mathbf{q}^{\theta_q}(\mathbf{v}), \mathbf{v}^{\theta_v}(\mathbf{v}))$ as

$$\frac{\partial \mathbf{F}_1}{\partial \mathbf{v}} = -\delta t\, \theta_q \theta_{vq} \mathbf{K}(\mathbf{q}^{\theta_q}, \mathbf{v}^{\theta_v}) - \theta_v \mathbf{D}(\mathbf{q}^{\theta_q}, \mathbf{v}^{\theta_v}),$$

with $\mathbf{K}$ and $\mathbf{D}$ the stiffness and damping matrices defined by Eqs. (12)-(13).

We can now write the Jacobian of $\mathbf{m}(\mathbf{v})$ in Eq. (26) as

$$\frac{\partial \mathbf{m}}{\partial \mathbf{v}} = \mathbf{A} + \mathbf{E} - \delta t \frac{\partial \mathbf{F}_2}{\partial \mathbf{v}},$$

where we defined

$$\mathbf{A} = \mathbf{M} + \delta t^2 \theta_q \theta_{qv} \mathbf{K} + \delta t \theta_v \mathbf{D}.$$

With these definitions the Taylor expansion in Eq. (26) becomes

$$\begin{aligned}\frac{\partial \mathbf{m}}{\partial \mathbf{v}}(\mathbf{v}-\mathbf{v}^*) &= \mathbf{A}(\mathbf{v}-\mathbf{v}^*) + \mathbf{E}(\mathbf{v}-\mathbf{v}^*) \\ &\quad - \delta t \frac{\partial \mathbf{F}_2}{\partial \mathbf{v}}(\mathbf{v}-\mathbf{v}^*) + \mathcal{O}_m(\|\mathbf{v}-\mathbf{v}^*\|^2).\end{aligned}$$

Since contact is compliant, forces are finite within the finite interval δt and therefore $\|\mathbf{v}-\mathbf{v}^*\| = \mathcal{O}(\delta t)$. Thus

$$\begin{aligned}\mathbf{E}(\mathbf{v}-\mathbf{v}^*) &= \mathcal{O}_E(\delta t^3), \\ \delta t \frac{\partial \mathbf{F}_2}{\partial \mathbf{v}}(\mathbf{v}-\mathbf{v}^*) &= \mathcal{O}_G(\delta t^2), \\ \mathcal{O}_m(\|\mathbf{v}-\mathbf{v}^*\|^2) &= \mathcal{O}_m(\delta t^2).\end{aligned}$$

Therefore, the positive definite linearization

$$\mathbf{A}(\mathbf{v}-\mathbf{v}^*) + \mathcal{O}_E(\delta t^3) + \mathcal{O}_G(\delta t^2) + \mathcal{O}_m(\delta t^2) = \mathbf{J}^T\boldsymbol{\gamma},$$

agrees with the original momentum balance in Eq. (7) to second order.

Finally, notice that $\mathbf{A}$ is a linear combination of positive definite matrices with non-negative scalars in the linear combination, and therefore $\mathbf{A} \succ 0$. ■

APPENDIX B
PROOF OF THEOREM 1

The Lagrangian of the primal formulation in Eq. (15) is

$$\mathcal{L}(\mathbf{v}, \boldsymbol{\sigma}, \boldsymbol{\gamma}) = \frac{1}{2}\|\mathbf{v}-\mathbf{v}^*\|_A^2 + \frac{1}{2}\|\boldsymbol{\sigma}\|_R^2 - \boldsymbol{\gamma}^T\mathbf{g}, \tag{27}$$

with $\boldsymbol{\gamma} \in \mathcal{F}$ the dual variable to enforce the constraint $\boldsymbol{g} \in \mathcal{F}^*$. Minimizing the Lagrangian jointly in variables $\mathbf{v}$ and $\boldsymbol{\sigma}$ leads to the optimality conditions

$$\mathbf{A}(\mathbf{v}-\mathbf{v}^*) = \mathbf{J}^T\boldsymbol{\gamma} \tag{28a}$$

$$\boldsymbol{\sigma} = \boldsymbol{\gamma}. \tag{28b}$$

The optimality condition (28a) reveals that the multipliers $\boldsymbol{\gamma}$ are indeed the contact impulses, and we recover the balance of momentum. The optimality condition (28b) allows us to eliminate $\boldsymbol{\sigma}$. We then substitute these results back into the Lagrangian to recover the dual in (5)

$$\min_{\boldsymbol{\gamma}\in\mathcal{F}} \ell_d(\boldsymbol{\gamma}) = \frac{1}{2}\boldsymbol{\gamma}^T(\mathbf{W}+\mathbf{R})\boldsymbol{\gamma} + \boldsymbol{r}^T\boldsymbol{\gamma},$$

where, in contrast to previous work, our Delassus operator $\mathbf{W} = \mathbf{J}\mathbf{A}^{-1}\mathbf{J}^T$ now also contains the contribution of internal force elements (through Eq. (11)) and $\mathbf{r} = \mathbf{v}_c^* - \hat{\mathbf{v}}_c$ with $\mathbf{v}_c^* = \mathbf{J}\mathbf{v}^*$. ■

APPENDIX C
PROOF OF THEOREM 2

Before proving this theorem, we need the following result.

Lemma 1. *The conic constraint $\mathbf{g}(\mathbf{v}, \boldsymbol{\sigma}) \in \mathcal{F}^*$ is satisfied if $\boldsymbol{\sigma}$ is given by $P_{\mathcal{F}}(\mathbf{y}(\mathbf{v}))$.*

Proof: Since $\boldsymbol{\sigma}$ is the projection of $\mathbf{y}(\mathbf{v})$ to the cone $\mathcal{F}$ with the $\mathbf{R}$ norm, by Moreau's decomposition theorem, we know that $\mathbf{y}(\mathbf{v}) - \boldsymbol{\sigma}$ is in the polar cone of $\mathcal{F}$ with the $\mathbf{R}$ norm. That is, $\langle \mathbf{y}(\mathbf{v}) - \boldsymbol{\sigma}, \mathbf{x}\rangle_{\mathbf{R}} \leq 0$ for all $\mathbf{x} \in \mathcal{F}$, with the inner product $\langle \mathbf{v}, \mathbf{w}\rangle_{\mathbf{R}} = \mathbf{v}^T\mathbf{R}\mathbf{w}$. Reorganizing terms, we get

$$\begin{aligned}\mathbf{x}^T\mathbf{R}(\mathbf{y}(\mathbf{v}) - \boldsymbol{\sigma}) &\leq 0, \\ \mathbf{x}^T(-\mathbf{R}\boldsymbol{\sigma} - \mathbf{v}_c + \hat{\mathbf{v}}_c) &\leq 0, \\ \langle \mathbf{x}, -\mathbf{R}\boldsymbol{\sigma} - \mathbf{v}_c + \hat{\mathbf{v}}_c\rangle &\leq 0,\end{aligned}$$

for all $\mathbf{x} \in \mathcal{F}$. Therefore, it follows that $-\mathbf{g} = -(\mathbf{v}_c - \hat{\mathbf{v}}_c + \mathbf{R}\boldsymbol{\sigma})$ is in the polar cone of $\mathcal{F}$ and thus $\mathbf{g}$ is in the dual cone of $\mathcal{F}$. ■

The optimality condition for the unconstrained formulation in (17) is $\nabla \ell_p(\mathbf{v}) = \mathbf{0}$. It is shown in Appendix E that

$$\nabla \ell_p(\mathbf{v}) = \mathbf{A}(\mathbf{v} - \mathbf{v}^*) - \mathbf{J}^T \boldsymbol{\gamma}(\mathbf{v}),$$

with impulses given by $\boldsymbol{\gamma}(\mathbf{v}) = P_{\mathcal{F}}(\mathbf{y}(\mathbf{v}))$, the dual optimal. Therefore, $\nabla \ell_p(\mathbf{v}) = \mathbf{0}$ implies (28a), the first optimality condition for (15).

The analytical inverse dynamics solution shows that $\boldsymbol{\gamma} = P_{\mathcal{F}}(\mathbf{y}(\mathbf{v}))$ with the primal optimal $\mathbf{v}$. Hence, choosing $\boldsymbol{\sigma} = P_{\mathcal{F}}(\mathbf{y}(\mathbf{v}))$ with the primal optimal $\mathbf{v}$ satisfies (28b), the second optimality condition for (15).

Finally, by Lemma 1, the cone constraint $\mathbf{g}(\mathbf{v}, \boldsymbol{\sigma}) \in \mathcal{F}^*$ is satisfied. ■

Appendix D
Analytical Inverse Dynamics

We perform the projection in Eq. (16) for a regularization of the form $\boldsymbol{R} = \text{diag}([R_t, R_t, R_n])$. For simplicity, we drop contact subindex i. We make the change of variables $\tilde{\boldsymbol{\gamma}} = \boldsymbol{R}^{1/2}\boldsymbol{\gamma}$ and $\tilde{\boldsymbol{y}} = \boldsymbol{R}^{1/2}\boldsymbol{y}$ [16], and observe that $\tilde{\boldsymbol{\gamma}}$ is the Euclidian projection of $\tilde{\boldsymbol{y}}$ onto cone $\tilde{\mathcal{F}}$ with coefficient $\tilde{\mu} = \mu\,(R_t/R_n)^{1/2}$. We conclude that

$$P_{\mathcal{F}}(\boldsymbol{y}) = \boldsymbol{R}^{-1/2} P_{\tilde{\mathcal{F}}}(\tilde{\boldsymbol{y}}),$$

We partition $\mathbb{R}^3$ into three regions, see Fig. 22: closed cone $\tilde{\mathcal{F}}$, denoted with $\mathcal{R}_I$, the interior of the polar $\tilde{\mathcal{F}}^\circ$, denoted with $\mathcal{R}_{III}$, and the remaining area, which we denote with $\mathcal{R}_{II}$. For $\tilde{\boldsymbol{y}} \in \mathcal{R}_I$ we simply have that $P_{\tilde{\mathcal{F}}}(\tilde{\boldsymbol{y}}) = \tilde{\boldsymbol{y}}$. When $\tilde{\boldsymbol{y}} \in \mathcal{R}_{III}$, $P_{\tilde{\mathcal{F}}}(\tilde{\boldsymbol{y}}) = \mathbf{0}$. Finally, when $\tilde{\boldsymbol{y}} \in \mathcal{R}_{II}$, we evaluate $P_{\tilde{\mathcal{F}}}(\tilde{\boldsymbol{y}})$ via Euclidean projection onto the boundary of $\tilde{\mathcal{F}}$, which admits a simple formula. We define $\hat{\boldsymbol{f}} = [\tilde{\mu}\hat{\boldsymbol{t}}, 1]/\sqrt{1+\tilde{\mu}^2}$, the unit vector along the wall of the cone shown in Fig. 22, with $\hat{\boldsymbol{t}} = \tilde{\boldsymbol{y}}_t/\|\tilde{\boldsymbol{y}}_t\| = \boldsymbol{y}_t/\|\boldsymbol{y}_t\|$. Then the projection is computed as $\tilde{\boldsymbol{\gamma}} = (\tilde{\boldsymbol{y}} \cdot \hat{\boldsymbol{f}})\hat{\boldsymbol{f}}$. After some algebraic manipulation we have that $P_{\tilde{\mathcal{F}}}(\tilde{\boldsymbol{y}}) = [\tilde{\boldsymbol{\gamma}}_t, \tilde{\gamma}_n]$ with

$$\begin{aligned}\tilde{\boldsymbol{\gamma}}_t &= \tilde{\mu}\tilde{\gamma}_n \hat{\boldsymbol{t}},\\ \tilde{\gamma}_n &= \frac{1}{1+\tilde{\mu}^2}\left(\tilde{y}_n + \tilde{\mu}\tilde{y}_r\right),\end{aligned}$$

where $\tilde{y}_r = \|\tilde{\boldsymbol{y}}_t\|$. Note that this formula is well-defined on $\mathcal{R}_{II}$, since $\boldsymbol{y}_t = \mathbf{0}$ only if $\boldsymbol{y}$ is in regions $\mathcal{R}_I$ or $\mathcal{R}_{III}$.

Finally, we apply the inverse transformation $\boldsymbol{\gamma} = \mathbf{R}^{-1/2} P_{\tilde{\mathcal{F}}}(\tilde{\boldsymbol{y}})$ and after some algebraic manipulation we recover the projection $\boldsymbol{\gamma} = P_{\mathcal{F}}(\boldsymbol{y})$ in Eq. (18).

Appendix E
Computation of the Gradients

We will start by taking derivatives of the regularizer term ℓ_R. First we notice that we can write this term as

$$\ell_R = \frac{1}{2}\|\boldsymbol{\gamma}\|_R^2 = \sum_i \ell_{R_i},$$

with $\ell_{R_i} = 1/2\|\boldsymbol{\gamma}_i\|_{R_i}^2$. Since $\nabla_{\boldsymbol{y}_j}\ell_{R_i} = \mathbf{0}$ for $i \neq j$, we only need to compute the gradients of $\ell_{R_i}(\mathbf{y})$ with respect to the contact point variable $\boldsymbol{y}_i \in \mathbb{R}^3$. Dropping contact subindex i for simplicity, we write the regularization as

$$\ell_R = \frac{1}{2}\|\boldsymbol{\gamma}\|_R^2 = \frac{1}{2}(R_t\|\boldsymbol{\gamma}_t\|^2 + R_n\gamma_n^2).$$

We use Eq. (18) to write the cost in terms of $\boldsymbol{y}$ as

$$\ell_R(\boldsymbol{y}) = \begin{cases} \dfrac{1}{2}(R_t y_r^2 + R_n y_n^2) & \text{stiction, } y_r \le \mu y_n \\ \dfrac{R_n}{2(1+\tilde{\mu}^2)}\left(y_n + \hat{\mu} y_r\right)^2 & \text{sliding, } -\hat{\mu}y_r < y_n \le \dfrac{y_r}{\mu} \\ \mathbf{0} & \text{no contact, } y_n < -\hat{\mu}y_r \end{cases} \tag{29}$$

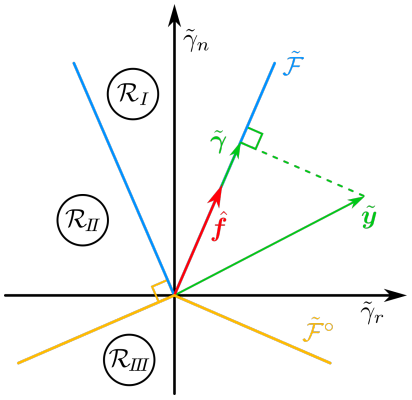

Fig. 22: Geometry of the projection and regions in the $\tilde{\boldsymbol{y}}$ space.

A. Gradients per Contact Point

We use the following identities to simplify expressions

$$\frac{\partial y_r}{\partial \boldsymbol{y}_t} = \hat{\boldsymbol{t}}, \quad \frac{\partial \hat{\boldsymbol{t}}}{\partial \boldsymbol{y}_t} = \frac{\boldsymbol{P}^\perp(\hat{\boldsymbol{t}})}{y_r},$$

where the 2×2 projection matrix is

$$\boldsymbol{P}^\perp(\hat{\boldsymbol{t}}) = \boldsymbol{I}_2 - \boldsymbol{P}(\hat{\boldsymbol{t}}), \quad \text{with } \boldsymbol{P}(\hat{\boldsymbol{t}}) = \hat{\boldsymbol{t}} \otimes \hat{\boldsymbol{t}}.$$

Taking the gradient of Eq. (29) results in

$$\nabla_{\boldsymbol{y}}\ell_R(\boldsymbol{y}) = \begin{cases} \boldsymbol{R}\,\boldsymbol{y} & \text{stiction, } y_r \le \mu y_n \\ \dfrac{1}{1+\tilde{\mu}^2}\hat{s}^\circ(\boldsymbol{y})\begin{bmatrix}\mu R_t \hat{\boldsymbol{t}} \\ R_n\end{bmatrix} & \text{sliding, } -\hat{\mu}y_r < y_n \le \dfrac{y_r}{\mu} \\ \mathbf{0} & \text{no contact, } y_n < -\hat{\mu}y_r \end{cases} \tag{30}$$

with $\hat{s}^\circ(\boldsymbol{y}) = \hat{\mu}y_r + y_n$ positive in the sliding region. We note that $\nabla_{\boldsymbol{y}}\ell_R(\boldsymbol{y})$ is not differentiable at the boundaries of $\mathcal{F}$ and $\mathcal{F}^\circ$. At points of differentiability, the Hessian $\nabla^2_{\boldsymbol{y}}\ell_R(\boldsymbol{y})$ is computed by taking derivatives of Eq. (30)

$$\nabla^2_{\boldsymbol{y}}\ell_R(\boldsymbol{y}) = \begin{cases} \boldsymbol{R} & \text{stiction,} \\ \dfrac{R_n}{1+\tilde{\mu}^2}\begin{bmatrix}\hat{\mu}\left(\hat{\mu}\boldsymbol{P}(\hat{\boldsymbol{t}}) + \hat{s}^\circ(\boldsymbol{y})\boldsymbol{P}^\perp(\hat{\boldsymbol{t}})/y_r\right) & \hat{\mu}\hat{\boldsymbol{t}} \\ \hat{\mu}\hat{\boldsymbol{t}}^T & 1\end{bmatrix} & \text{sliding,} \\ \mathbf{0} & \text{no contact.} \end{cases} \tag{31}$$

Clearly in the stiction region we have $\nabla^2_{\boldsymbol{y}}\ell_R(\boldsymbol{y}) \succ 0$. Since in the stiction region we have $\hat{s}^\circ(\boldsymbol{y}) > 0$, the linear

combination of $\boldsymbol{P}(\hat{\boldsymbol{t}})$ and $\boldsymbol{P}(\hat{\boldsymbol{t}})^{\perp}$ in Eq. (31) is PSD (since both projection matrices are PSD). Therefore $\nabla^2_{\boldsymbol{y}}\ell_R(\boldsymbol{y}) \succeq 0$.

B. Gradients with Respect to Velocities

Recall we use bold italics for vectors in $\mathbb{R}^3$ and non-italics bold for their stacked counterpart. With $\mathbf{y} = -\mathbf{R}^{-1}(\mathbf{J}\mathbf{v} - \hat{\mathbf{v}}_c)$ we use the chain rule to compute the gradient in terms of velocities

$$\nabla_{\mathbf{v}}\ell_R = -\mathbf{J}^T\mathbf{R}^{-1}\nabla_{\mathbf{y}}\ell_R, \tag{32}$$

which, using Eq. (30), can be shown to equal

$$\nabla_{\mathbf{v}}\ell_R = -\mathbf{J}^T\boldsymbol{\gamma}, \tag{33}$$

At points of differentiability, we obtain the Hessian of the regularizer $\ell_R(\mathbf{v})$ from the gradient of $\boldsymbol{\gamma}(\mathbf{v})$ in Eq. (33)

$$\nabla^2_{\mathbf{v}}\ell_R(\mathbf{v}) = -\mathbf{J}^T\nabla_{\mathbf{v}_c}\boldsymbol{\gamma}\,\mathbf{J},$$
$$\nabla_{\mathbf{v}_c}\boldsymbol{\gamma} = -\nabla_{\mathbf{y}}\boldsymbol{\gamma}\mathbf{R}^{-1},$$

where $\nabla_{\mathbf{v}_c}\boldsymbol{\gamma}$ is a block diagonal matrix where each diagonal block is the 3×3 matrix $\nabla_{\mathbf{v}_{c,i}}\boldsymbol{\gamma}_i$ for the i-th contact. Alternatively, taking the gradient of Eq. (32) leads to the equivalent result

$$\nabla^2_{\mathbf{v}}\ell_R = \mathbf{J}^T\mathbf{R}^{-1}\nabla^2_{\mathbf{y}}\ell_R\mathbf{R}^{-1}\mathbf{J},$$

where we can verify indeed that $-\nabla_{\mathbf{v}_c}\boldsymbol{\gamma} = \mathbf{R}^{-1}\nabla^2_{\mathbf{y}}\ell_R\mathbf{R}^{-1}$. Since $\nabla^2_{\mathbf{y}}\ell_R \succeq 0$, it follows that $-\nabla_{\mathbf{v}_c}\boldsymbol{\gamma} \succeq 0$.

We define $\boldsymbol{G}_i \in \mathbb{R}^{3\times 3}$ the matrix that evaluates to $-\nabla_{\mathbf{v}_{c,i}}\boldsymbol{\gamma}_i$ within regions $\mathcal{R}_I$, $\mathcal{R}_{II}$ and $\mathcal{R}_{III}$ where the projection is differentiable. At the boundary of $\mathcal{F}$ we use the analytical expression from $\mathcal{R}_I$. At the boundary of $\mathcal{F}^{\circ}$ we use the analytical expression from $\mathcal{R}_{II}$. This extension fully specifies $\boldsymbol{G}_i$ for all $\boldsymbol{y}_i \in \mathbb{R}^3$. Finally, we define the $3n_c \times 3n_c$ matrix $\mathbf{G} = \mathrm{diag}(\boldsymbol{G}_i) \succeq 0$.

C. Gradients of the Primal Cost

With these results, we can now write the gradient $\nabla_{\boldsymbol{v}}\ell_p$ and weighting matrix $\mathbf{H}$ in Algorithm 1. For the gradient we have

$$\nabla_{\mathbf{v}}\ell_p(\mathbf{v}) = \mathbf{A}(\mathbf{v} - \mathbf{v}^*) + \nabla_{\mathbf{v}}\ell_R.$$

which using Eq. (33) can be written as

$$\nabla_{\mathbf{v}}\ell_p(\mathbf{v}) = \mathbf{A}(\mathbf{v} - \mathbf{v}^*) - \mathbf{J}^T\boldsymbol{\gamma},$$

and since the unconstrained minimization seeks to satisfy the optimality condition $\nabla_{\mathbf{v}}\ell_p = \mathbf{0}$, we recover the balance of momentum.

Finally, we define the weighting matrix $\mathbf{H}$ as

$$\mathbf{H} = \mathbf{A} + \mathbf{J}^T\mathbf{G}\,\mathbf{J},$$

which, given the definition of $\mathbf{G}$, returns the Hessian of $\ell_p(\boldsymbol{v})$ when the gradient is differentiable and extends the analytical expressions at points of non-differentiability. Since $\mathbf{A} \succ 0$ and $\mathbf{G} \succeq 0$, we have $\mathbf{H} \succ 0$.

APPENDIX F
CONVERGENCE ANALYSIS OF SAP

Convergence of SAP is established by first showing that the objective function $\ell_p(\mathbf{v}) = \frac{1}{2}\|\mathbf{v} - \mathbf{v}^*\|^2_A + P_{\mathcal{F}}(\mathbf{y}(\mathbf{v}))\|^2_R$ is *strongly convex* and differentiable with *Lipschitz continuous* gradients. The former property is inherited from the positive-definite quadratic term provided by the positive definite matrix $\mathbf{A}$ in Eq. (17). The latter is shown using differentiability of the squared-distance function and the Lipschitz continuity of its gradient map (Theorems 5.3-i 6.1-i of [43]) combined with the identity

$$d^2_{\mathcal{K}^{\circ}}(x) = \|P_{\mathcal{K}}(x)\|^2_{\mathbf{R}},$$

for any closed, convex cone $\mathcal{K}$. Here the distance and projection functions are with respect to the norm $\|\cdot\|_{\mathbf{R}}$, while $\mathcal{K}^{\circ}$ denotes the polar cone with respect to the corresponding inner-product $\mathbf{x}^T\mathbf{R}\mathbf{y}$.

Lemma 2. *The following statements hold.*

- *The function $\ell_p(\mathbf{v})$ is strongly convex, i.e., there exists $\mu > 0$ such that*

$$\ell_p(\mathbf{u}) \geq \ell_p(\mathbf{v}) + \nabla\ell_p(\mathbf{v})(\mathbf{u} - \mathbf{v}) + \frac{\mu}{2}\|\mathbf{u} - \mathbf{v}\|^2$$

- *The function $\ell_p(\mathbf{v})$ is differentiable and has Lipschitz continuous gradients, i.e., $\nabla\ell_p(\mathbf{v})$ exists for all $\mathbf{v}$ and there exists $L \geq 0$ satisfying*

$$\|\nabla\ell_p(\mathbf{v}) - \nabla\ell_p(\mathbf{u})\| \leq L\|\mathbf{u} - \mathbf{v}\|$$

Proof. The objective $\ell_p(\mathbf{v})$ is a function $f : \mathbb{R}^n \to \mathbb{R}$ of the following form

$$f(\mathbf{v}) = \frac{1}{2}d^2_{\mathcal{K}}(\mathbf{Z}\mathbf{v} + \mathbf{b}) + \mathbf{v}^T\mathbf{W}\mathbf{v} + \mathbf{q}^T\mathbf{v},$$

where $\mathbf{Z} \in \mathbb{R}^{m\times n}$, $\mathbf{W} \in \mathbb{R}^{n\times n}$ is symmetric and positive definite, and $d_{\mathcal{K}} : \mathbb{R}^m \to \mathbb{R}$ denotes the distance function of a closed, convex set $\mathcal{K} \subseteq \mathbb{R}^m$ as measured by some quadratic norm $\|\mathbf{x}\|_Q$, i.e.,

$$d_{\mathcal{K}}(\mathbf{v}) = \inf\{\|\mathbf{v} - \mathbf{z}\|_Q : \mathbf{z} \in \mathcal{K}\}.$$

The sum of a strongly convex function with a convex function is strongly convex. Since the squared distance function is convex, and the quadratic term $\mathbf{v}^T\mathbf{W}\mathbf{v}$ is strongly convex (given that $\mathbf{W} \succ 0$), the first statement holds.

The second statement follows trivially if we can show it holds for the squared distance function. Differentiability follows from Chapter 4 (Theorems 5.3-i 6.1-i) of [43], which shows that

$$\nabla d^2_{\mathcal{K}}(\mathbf{v}) = 2\mathbf{Q}(\mathbf{v} - P_{\mathcal{K}}(\mathbf{v})).$$

That the gradient of $d^2_{\mathcal{K}}(\mathbf{v})$ is Lipschitz follows from Lipschitz continuity of projection maps onto closed, convex sets. ■

We remark that strong convexity implies the reverse Lipschitz inequality $\|\nabla f(\mathbf{v}) - \nabla f(\mathbf{u})\| \geq \mu\|\mathbf{v} - \mathbf{u}\|$, which in turn means that the parameter μ and the Lipschitz constant L satisfy $\mu \leq L$.

Recall that SAP (Algorithm 1) is a special case of the following iterative method for minimizing a function $f : \mathbb{R}^n \to \mathbb{R}$

given some initial point $\mathbf{v}_0 \in \mathbb{R}^n$:

$$\begin{aligned} \mathbf{d}_m &= -\mathbf{H}^{-1}(\mathbf{v}_m)\nabla f(\mathbf{v}_m), \\ t_m &= \arg\min_t f(\mathbf{v}_m + t\mathbf{d}_m), \\ \mathbf{v}_{m+1} &= \mathbf{v}_m + t_m\mathbf{d}_m, \end{aligned} \tag{34}$$

where $\mathbf{H} : \mathbb{R}^n \to \mathbb{R}^{n\times n}$ is a function into the set of symmetric positive definite matrices, i.e., $\mathbf{H}(\mathbf{v}) = \mathbf{H}(\mathbf{v})^T$ and $\mathbf{H}(\mathbf{v}) \succ 0$ for all $\mathbf{v} \in \mathbb{R}^n$. It is well known that gradient descent exhibits linear convergence to the global minimum when applied to a strongly convex function with Lipschitz continuous gradient. Incorporating a condition number bound σ for $\mathbf{H}(\mathbf{v})$ into standard gradient-descent analysis will prove that the iterations (34) also have linear convergence. To show this, we let $\text{cond}(\mathbf{H}(\mathbf{v}))$ denote the condition number of $\mathbf{H}(\mathbf{v})$ and $S(\mathbf{v}_0)$ denote the sub-level set $\{\mathbf{v} \in \mathbb{R}^n : f(\mathbf{v}) \le f(\mathbf{v}_0)\}$.

Lemma 3. *Let $f : \mathbb{R}^n \to \mathbb{R}$ be strongly convex and differentiable with Lipschitz-continuous gradients. Fix $\mathbf{v}_0 \in \mathbb{R}^n$. If there exists $\sigma > 0$ such that $\text{cond}(\mathbf{H}(\mathbf{v})) \le \sigma$ for all $\mathbf{v} \in S(\mathbf{v}_0)$, then the iterations (34) converge to the global minimum $\mathbf{v}_*$ of $f(\mathbf{v})$ when initialized at $\mathbf{v}_0$. Moreover,*

$$f(\mathbf{v}_m) - f(\mathbf{v}_*) \le (1 - \frac{\mu}{\sigma^2 L})^m (f(\mathbf{v}_0) - f(\mathbf{v}_*))$$

for all iterations m, where μ is the strong-convexity parameter of $f(\mathbf{v})$ and L is the Lipschitz constant of $\nabla f(\mathbf{v})$.

Proof. Dropping the subscript m from $(\mathbf{v}_m, t_m, \mathbf{d}_m)$, we first observe that

$$f(\mathbf{v} + t\mathbf{d}) \le f(\mathbf{v}) + \langle \nabla f(\mathbf{v}), \mathbf{d}\rangle t + \frac{L}{2}\|\mathbf{d}\|^2 t^2,$$

by Lipschitz continuity. Substituting $\mathbf{d} = -\mathbf{H}^{-1}\nabla f(\mathbf{v})$ gives

$$f(\mathbf{v}+t\mathbf{d}) = f(\mathbf{v}) - \nabla f(\mathbf{v})^T \mathbf{H}^{-1}\nabla f(\mathbf{v}) t + \frac{L}{2}\|\mathbf{H}^{-1}\nabla f(\mathbf{v})\|^2 t^2.$$

Letting λ_{max} and λ_{min} denote the maximum and minimum eigenvalues of $\mathbf{H}$ evaluated at $\mathbf{v}$, it also follows that

$$f(\mathbf{v} + t\mathbf{d}) \le f(\mathbf{v}) - \frac{1}{\lambda_{\max}}\|\nabla f(\mathbf{v})\|^2 t + \frac{L}{2}\frac{1}{\lambda_{\min}^2}\|\nabla f(\mathbf{v})\|^2 t^2.$$

Letting $\bar{t}$ denote the minimizer of the right-hand-side, we conclude that

$$f(\mathbf{v} + t\mathbf{d}) \le f(\mathbf{v} + \bar{t}\mathbf{d}) \le f(\mathbf{v}) - \frac{1}{2}(\frac{\lambda_{\min}^2}{\lambda_{\max}^2 L}\|\nabla f(\mathbf{v})\|^2),$$

where the first inequality follows from the exact line search used to select t. Since $\sigma^2 \ge \lambda_{\max}^2/\lambda_{\min}^2$, we conclude that

$$f(\mathbf{v} + t\mathbf{d}) \le f(\mathbf{v}) - \frac{1}{2\sigma^2 L}\|\nabla f(\mathbf{v})\|^2.$$

On the other hand, letting $f_* = f(\mathbf{v}_*)$ we have from strong convexity that the Polyak-Lojasiewicz inequality holds:

$$\|\nabla f(\mathbf{v})\|^2 \ge 2\mu(f(\mathbf{v}) - f_*).$$

Hence,

$$f(\mathbf{v} + t\mathbf{d}) \le f(\mathbf{v}) - \frac{\mu}{\sigma^2 L}(f(\mathbf{v}) - f_*).$$

Subtracting f_* from both sides and factoring shows

$$f(\mathbf{v} + t\mathbf{d}) - f_* \le (1 - \frac{\mu}{\sigma^2 L})(f(\mathbf{v}) - f_*).$$

It follows that each iteration m satisfies

$$f(\mathbf{v}_{m+1}) - f_* \le (1 - \frac{\mu}{\sigma^2 L})^m (f(\mathbf{v}_0) - f_*).$$

Since $\sigma \ge 1$ and $L \ge \mu$, the iterations converge, and the proof is completed. ∎

Combining these lemmas shows that SAP globally converges at (at least) a linear rate. By observing that SAP reduces to Newton's method when the gradient is differentiable, we can also prove local quadratic convergence assuming differentiability on a neighborhood of the optimum $\mathbf{v}_*$.

Theorem 3. *The following statements hold.*

- *SAP globally converges from all initial conditions.*
- *If $\nabla f(\mathbf{v})$ is differentiable on the ball $B(\mathbf{v}_*, r) := \{\mathbf{v} : \|\mathbf{v} - \mathbf{v}_*\| \le r\}$ for some $r > 0$, then SAP exhibits quadratic convergence, i.e., for some finite M and $\zeta > 0$*

$$\|\mathbf{v}_m - \mathbf{v}_*\| \le \zeta \|\mathbf{v}_{m+1} - \mathbf{v}_*\|^2$$

for all $m > M$.

Proof. The first statement follows from Lemmas 2 and 3.

To prove the second, we show that $B(\mathbf{v}_*, r)$ contains a sublevel set $\Omega_\beta = \{\mathbf{v} : f(\mathbf{v}) \le \beta\}$ for some $\beta > 0$, implying that SAP reduces to Newton's method with exact line search for some $m > M$, given that sublevel sets are invariant.

To begin, we have, by strong convexity, that

$$\beta \ge f(\mathbf{v}) \ge f(\mathbf{v}_*) + \frac{\mu}{2}\|\mathbf{v} - \mathbf{v}_*\|^2, \tag{35}$$

for all $\mathbf{v} \in \Omega_\beta$. Rearranging shows that

$$\|\mathbf{v} - \mathbf{v}_*\|^2 \le 2\frac{\beta - f(\mathbf{v}_*)}{\mu}.$$

Hence, $B(\mathbf{v}_*, r)$ contains Ω_β for any β satisfying $2\frac{\beta - f(\mathbf{v}_*)}{\mu} < r$. For some finite M, we also have that $v_m \in \Omega_\beta$ for all $m > M$ by Lemma 3.

Next, we prove that Newton iterations are quadratically convergent with exact line search. Indeed, using once more the strong convexity result in Eq. (35)

$$\begin{aligned} \|\mathbf{v}_{m+1} - \mathbf{v}_*\|^2 &\le \frac{2}{\mu}(f(\mathbf{v}_{m+1}) - f(\mathbf{v}_*)) \\ &= \frac{2}{\mu}(f(\mathbf{v}_m + t_m\mathbf{d}_m) - f(\mathbf{v}_*)) \\ &\le \frac{2}{\mu}(f(\mathbf{v}_m + \mathbf{d}_m) - f(\mathbf{v}_*)) \\ &\le \frac{2}{\mu}L\|\mathbf{v}_m + \mathbf{d}_m - \mathbf{v}_*\|^2, \end{aligned}$$

where the first line uses strong convexity, the third exact line search, and the last Lipschitz continuity. But for some $\kappa > 0$, we have that $\|\mathbf{v}_m + \mathbf{d}_m - \mathbf{v}_*\|^2 \le \kappa\|\mathbf{v}_m - \mathbf{v}_*\|^4$ by quadratic convergence of Newton's method with unit step-size ([35, Theorem 3.5]). Hence,

$$\|\mathbf{v}_{m+1} - \mathbf{v}_*\|^2 \le \frac{2}{\mu}L\kappa\|\mathbf{v}_m - \mathbf{v}_*\|^4,$$

and the claim is proven. ■

ACKNOWLEDGMENT

The authors would like to thank especially to Michael Sherman for his trust on this research from day one and to the Dynamics & Simulation and Dexterous Manipulation teams at TRI for their continuous patience and support.

REFERENCES

[1] D. Baraff, "Issues in computing contact forces for non-penetrating rigid bodies," *Algorithmica*, vol. 10, no. 2, pp. 292–352, 1993.

[2] S. Hogan and K. U. Kristiansen, "On the regularization of impact without collision: the painlevé paradox and compliance," *Proceedings of the Royal Society A: Mathematical, Physical and Engineering Sciences*, vol. 473, no. 2202, p. 20160773, 2017.

[3] J.-S. Pang and D. E. Stewart, "Differential variational inequalities," *Mathematical programming*, vol. 113, no. 2, pp. 345–424, 2008.

[4] E. J. Haug, S. C. Wu, and S. M. Yang, "Dynamics of mechanical systems with coulomb friction, stiction, impact and constraint addition-deletion—i theory," *Mechanism and Machine Theory*, vol. 21, no. 5, pp. 401–406, 1986.

[5] D. E. Stewart and J. C. Trinkle, "An implicit time-stepping scheme for rigid body dynamics with inelastic collisions and coulomb friction," *International Journal for Numerical Methods in Engineering*, vol. 39, no. 15, pp. 2673–2691, 1996.

[6] M. Anitescu and F. A. Potra, "Formulating dynamic multi-rigid-body contact problems with friction as solvable linear complementarity problems," *Nonlinear Dynamics*, vol. 14, no. 3, pp. 231–247, 1997.

[7] D. E. Stewart, "Convergence of a time-stepping scheme for rigid-body dynamics and resolution of painlevé's problem," *Archive for Rational Mechanics and Analysis*, vol. 145, no. 3, pp. 215–260, 1998.

[8] D. M. Kaufman, S. Sueda, D. L. James, and D. K. Pai, "Staggered projections for frictional contact in multibody systems," *ACM Trans. Graph.*, vol. 27, no. 5, Dec. 2008.

[9] D. Baraff, "Fast contact force computation for nonpenetrating rigid bodies," in *Proceedings of the 21st annual conference on Computer graphics and interactive techniques*, 1994, pp. 23–34.

[10] C. Duriez, F. Dubois, A. Kheddar, and C. Andriot, "Realistic haptic rendering of interacting deformable objects in virtual environments," *IEEE transactions on visualization and computer graphics*, vol. 12, no. 1, pp. 36–47, 2006.

[11] E. Coumans and Y. Bai, "Pybullet, a python module for physics simulation for games, robotics and machine learning," http://pybullet.org, 2016–2020.

[12] K. Erleben, "Velocity-based shock propagation for multibody dynamics animation," *ACM Transactions on Graphics (TOG)*, vol. 26, no. 2, pp. 12–es, 2007.

[13] M. Anitescu, "Optimization-based simulation of nonsmooth rigid multibody dynamics," *Mathematical Programming*, vol. 105, no. 1, pp. 113–143, 2006.

[14] H. Mazhar, D. Melanz, M. Ferris, and D. Negrut, "An analysis of several methods for handling hard-sphere frictional contact in rigid multibody dynamics," Citeseer, Tech. Rep., 2014.

[15] E. Todorov, "A convex, smooth and invertible contact model for trajectory optimization," in *2011 IEEE International Conference on Robotics and Automation*. IEEE, 2011, pp. 1071–1076.

[16] ——, "Convex and analytically-invertible dynamics with contacts and constraints: Theory and implementation in mujoco," in *2014 IEEE International Conference on Robotics and Automation (ICRA)*. IEEE, 2014, pp. 6054–6061.

[17] D. Kang and J. Hwangho, "SimBenchmark. Physics engine benchmark for robotics applications: RaiSim vs. Bullet vs. ODE vs. MuJoCo vs. DartSim." https://leggedrobotics.github.io/SimBenchmark.

[18] R. Smith, "Open dynamics engine," http://www.ode.org/.

[19] J. Lee, M. X. Grey, S. Ha, T. Kunz, S. Jain, Y. Ye, S. S. Srinivasa, M. Stilman, and C. K. Liu, "Dart: Dynamic animation and robotics toolkit," *Journal of Open Source Software*, vol. 3, no. 22, p. 500, 2018.

[20] CM Labs Simulations, "Theory guide: Vortex software's multibody dynamics engine," https://www.cm-labs.com/vortexstudiodocumentation.

[21] "AGX Dynamics," https://www.algoryx.se/products/agx-dynamics.

[22] R. Tedrake and the Drake Development Team, "Drake: Model-based design and verification for robotics," https://drake.mit.edu, 2019.

[23] A. M. Castro, A. Qu, N. Kuppuswamy, A. Alspach, and M. Sherman, "A transition-aware method for the simulation of compliant contact with regularized friction," *IEEE Robotics and Automation Letters*, vol. 5, no. 2, pp. 1859–1866, 2020.

[24] A. Tasora, R. Serban, H. Mazhar, A. Pazouki, D. Melanz, J. Fleischmann, M. Taylor, H. Sugiyama, and D. Negrut, "Chrono: An open source multi-physics dynamics engine," T. Kozubek, Ed. Springer, 2016, pp. 19–49.

[25] E. Todorov, "MuJoCo," http://www.mujoco.org.

[26] A. Tasora and M. Anitescu, "A matrix-free cone complementarity approach for solving large-scale, nonsmooth, rigid body dynamics," *Computer Methods in Applied Mechanics and Engineering*, vol. 200, no. 5-8, pp. 439–453, 2011.

[27] M. Anitescu and A. Tasora, "An iterative approach for cone complementarity problems for nonsmooth dynamics," *Computational Optimization and Applications*, vol. 47, no. 2, pp. 207–235, 2010.

[28] R. Elandt, E. Drumwright, M. Sherman, and A. Ruina, "A pressure field model for fast, robust approximation of net contact force and moment between nominally rigid objects," in *2019 IEEE/RSJ International Conference on Intelligent Robots and Systems (IROS)*. IEEE, 2019, pp. 8238–8245.

[29] J. Li, G. Daviet, R. Narain, F. Bertails-Descoubes, M. Overby, G. E. Brown, and L. Boissieux, "An implicit frictional contact solver for adaptive cloth simulation," *ACM Transactions on Graphics (TOG)*, vol. 37, no. 4, pp. 1–15, 2018.

[30] E. Hairer, S. Nørsett, and G. Wanner, *Solving Ordinary Differential Equations I: Nonstiff Problems*, ser. Springer Series in Computational Mathematics. Springer Berlin Heidelberg, 2008.

[31] F. A. Potra, M. Anitescu, B. Gavrea, and J. Trinkle, "A linearly implicit trapezoidal method for integrating stiff multibody dynamics with contact, joints, and friction," *International Journal for Numerical Methods in Engineering*, vol. 66, no. 7, pp. 1079–1124, 2006.

[32] C. Duriez, F. Dubois, A. Kheddar, and C. Andriot, "Realistic haptic rendering of interacting deformable objects in virtual environments," *IEEE transactions on visualization and computer graphics*, vol. 12, no. 1, pp. 36–47, 2005.

[33] J. BELL, L. HOWELL, and P. Colella, "An efficient second-order projection method for viscous incompressible flow," in *10th Computational Fluid Dynamics Conference*, 1991, p. 1560.

[34] R. Featherstone, *Rigid body dynamics algorithms*. Springer, 2008.

[35] J. Nocedal and S. Wright, *Numerical optimization*. Springer Science & Business Media, 2006.

[36] W. H. Press, H. William, S. A. Teukolsky, A. Saul, W. T. Vetterling, and B. P. Flannery, *Numerical recipes 3rd edition: The art of scientific computing*. Cambridge university press, 2007.

[37] T. A. Davis, S. Rajamanickam, and W. M. Sid-Lakhdar, "A survey of direct methods for sparse linear systems," *Acta Numerica*, vol. 25, pp. 383–566, 2016.

[38] L. Smail, "Junction trees constructions in bayesian networks," in *Journal of Physics: Conference Series*, vol. 893, no. 1. IOP Publishing, 2017, p. 012056.

[39] F. Permenter, "A geodesic interior-point method for linear optimization over symmetric cones," *arXiv preprint arXiv:2008.08047*, 2020.

[40] J. Masterjohn, D. Guoy, J. Shepherd, and A. Castro, "Discrete approximation of pressure field contact patches," 2021, submitted to ICRA 2022. Preprint available at https://arxiv.org/abs/2110.04157.

[41] N. Kuppuswamy, A. Alspach, A. Uttamchandani, S. Creasey, T. Ikeda, and R. Tedrake, "Soft-bubble grippers for robust and perceptive manipulation," in *2020 IEEE/RSJ International Conference on Intelligent Robots and Systems (IROS)*. IEEE, 2020, pp. 9917–9924.

[42] J. Carpentier, R. Budhiraja, and N. Mansard, "Proximal and sparse resolution of constrained dynamic equations," in *Robotics: Science and Systems 2021*, 2021.

[43] M. C. Delfour and J.-P. Zolésio, *Shapes and geometries: metrics, analysis, differential calculus, and optimization*. SIAM, 2011.